

Anisotropic hp space-time adaptivity and goal-oriented error control for convection-dominated problems

Nils Margenberg ^{*} Marius Paul Bruchhäuser [†] Bernhard Endtmayer ^{‡§}

We present an anisotropic goal-oriented error estimator based on the Dual Weighted Residual (DWR) method for time-dependent convection-dominated problems. Using elementwise p -anisotropic finite element spaces, the estimator is elementwise separated with respect to the single directions in space and time. This naturally leads to adaptive, anisotropic hp -refinement (h -anisotropic refinement and elementwise anisotropic p -enrichment). We employ discontinuous elements in space and time, which are well suited for problems with high Péclet numbers. Efficiency and robustness of the underlying algorithm are demonstrated for different goal functionals. The directional error indicators quantify anisotropy of the solution with respect to the goal, and produce hp -refinements that efficiently capture sharp layers. Numerical examples in up to three spatial dimensions demonstrate the superior performance of the proposed method compared to isotropic h and hp adaptive refinement using established benchmarks for convection-dominated transport.

Keywords: anisotropic hp -adaptivity, goal-oriented error control, dual-weighted residual method, space-time finite elements

MSC (2020): 65M60, 65N50, 65M15, 65N15

1 Introduction

Goal-oriented adaptivity and anisotropic mesh refinement are established tools in the numerical solution of partial differential equations (PDEs). While each of these techniques has been studied extensively, their combination in the context of convection-dominated, time-dependent problems remains an area of active research. Convection-dominated transport problems are characterized by sharp layers and fronts that benefit greatly from anisotropic hp -adaptive, goal-oriented refinement. In particular, the development of directional error indicators offers new opportunities in space-time hp -adaptivity for further improvement with regard to accurate and efficient simulations. This work contributes to this development by building a framework that performs hp -anisotropic space-time refinement driven by goal-oriented error control.

The concept of hp -adaptive finite elements was pioneered by Babuška et al. [10, 45, 46, 47, 11]. The theoretical foundation was laid in the 1980s, where it was demonstrated that combining mesh refinement (h -refinement) and increasing polynomial order (p -enrichment) can achieve exponential convergence rates on so-called geometrically graded meshes [45, 46, 9]. First versions of a hp -adaptive code were introduced

^{*}University of Magdeburg, Institute for Analysis and Numerics, Universitätsplatz 2, 39104 Magdeburg, Germany, nils.margenberg@ovgu.de, (Corresponding Author)

[†]Helmut Schmidt University, Faculty of Mechanical and Civil Engineering, Holstenhofweg 85, 22043 Hamburg, Germany, bruchhaeuser@hsu-hh.de

[‡]Leibniz University Hannover, Institute for Applied Mathematics, Welfengarten 1, 30167 Hannover, Germany, endtmayer@ifam.uni-hannover.de

[§]Cluster of Excellence PhoenixD (Photonics, Optics, and Engineering – Innovation Across Disciplines), Leibniz University Hannover, Germany

by Devloo [32] as well as Ainsworth and Senior [3] in the late 1990s and later on by Demkowicz et al. introducing a fully automatic hp -adaptive strategy for elliptic problems [30]. For a review of different methods to decide between h and p refinement, we refer to [51]. For a short review to the development of implementing hp elements we refer to the monograph [31]. Moreover, the monograph of Schwab provides a treatment of p/hp -FEM theory [70].

For anisotropic refinement, Apel's analysis of anisotropic interpolation error estimates [5] laid the groundwork for stretched meshes aligned with layers. Picasso was an early contributor to apply an adaptive algorithm with anisotropic spatial and temporal refinement for time-dependent problems [60]. Since then, several approaches for the directional refinement decisions have been proposed and are well established, cf., e.g., [41, 73, 40, 55, 4, 26]. For a short overview of anisotropic refinement methods in finite elements, we refer to the review [69].

At the turn of the last millennium, Becker and Rannacher introduced the Dual Weighted Residual (DWR) method [18, 17], which uses the solution of an adjoint problem to weight local residuals and estimates errors in a specific quantity of interest. At the same time, Oden and Prudhomme formulated a similar framework [58]. These works established the principle of goal-oriented adaptivity for elliptic PDEs, whereby Becker and Rannacher's work [17] became the foundational reference for DWR-based adaptivity. Šolín and Demkowicz extended DWR to drive both h and p refinement decisions in elliptic problems [71]. In the last two decades, the DWR method was applied to many mathematical models based on PDEs, including fluid mechanics, wave propagation, structural mechanics, eigenvalue problems and many others, cf., e.g., [61, 68, 12, 63, 19, 75, 35]. For a review including detailed lists of references regarding different model problems, we refer to [13, 37].

With regard to (convection-dominated) transport problems, the three approaches described above have been successfully applied severally as well as in varying combinations among each other. The analysis of hp -adaptive algorithms for transport-dominated problems was pioneered by Houston, Schwab, and Süli [50, 49], who demonstrated exponential convergence of stabilized and discontinuous Galerkin methods. For convection-dominated problems, Melenk provided rigorous analysis to prove exponential convergence of hp -FEM for singularly perturbed problems using anisotropic mesh grading and p -enrichment [56]. Bittl and Kuzmin proposed an hp -adaptive flux-corrected transport algorithm for unsteady linear convection equations in [20]. For the development of DG methods on hp -anisotropic meshes for steady-state convection-diffusion-reaction equations we refer to [42, 43], and using additionally goal-oriented error control we refer to [44]. Regarding non-stationary convection-diffusion problems, an hp -adaptive discontinuous Galerkin method using an a posteriori error estimator for the error in the $L^2(H^1) + L^\infty(L^2)$ -type norm was developed in [25]. Anisotropic mesh refinement applied to convection-diffusion-reaction equations can be found in [6, 41, 40, 53]. For time-dependent convection-dominated problems, the DWR method combined with stabilization has been investigated by some of the authors for isotropic [24, 21, 23, 22] as well as anisotropic [15, 16] adaptive refinement. For high-order methods, Ceze and Fidkowski developed an anisotropic hp -adaptation strategy driven by adjoint error estimates [27]. Dolejší et al. developed space-time DWR-based refinement strategies for convection-diffusion-reaction (CDR) equations [33], adjusting both mesh anisotropy and polynomial degrees in space and time. For general reviews of convection-dominated problems and further references, we refer to [66, 52].

In this work, we develop a tensor-product space-time DG discretization with fully anisotropic hp -adaptivity, allowing independent h - and p -updates per spatial direction and in time. Within a DWR framework, we derive directional error indicators $\eta_{h,i}, \eta_\tau, i = 1, \dots, d$, and use them to develop a principled refinement policy that naturally yields refinement decisions on anisotropic polynomial enrichment and geometric refinement. The decision between these two options is made based on a local saturation indicator, cf., e.g., [51]. The algorithms use efficient transfer and integration procedures on anisotropically refined meshes, implemented in the finite element library deal.II [1] with shared-memory parallelism. To improve the time-to-solution, we empirically assess an h - and p -robust preconditioning strategy for the resulting space-time systems that remains effective under strong anisotropy. We target well-known challenges in the numerical simulation of convection-dominated problems:

1. Resolving thin boundary/interior layers and geometric singularities (e.g., the Fichera corner) without spurious oscillations;
2. Reducing computational cost by concentrating resolution where a goal functional, chosen by the user, is most sensitive;
3. Deciding between h and p *per direction* in accordance with local anisotropy and regularity;
4. Ensuring solver robustness for highly anisotropic meshes and high polynomial degrees;

We propose a goal-oriented, anisotropic hp space-time adaptive algorithm based on the DWR method. Its realization builds on Richter's work on splitting spatial error contributions [64], on subsequent extensions in the space-time setting [15], and on anisotropic p -adaptivity by Houston et al. [43, 44]. We integrate these techniques into a unified framework suitable for challenging, time-dependent, convection-dominated problems. The directional error decomposition and associated directional refinement policy are key to efficient hp -adaptation and distinguish our approach from methods that select an action via a "competition" among candidate refinements (see, for instance, [28]). By selecting h - or p -updates directly from the split estimator, we avoid candidate testing while aligning refinement with the local anisotropy.

The remainder of this work is structured as follows: In Sec. 2, we introduce the mathematical notation, the CDR equation, and its variational formulation. The discrete anisotropic finite element spaces are introduced in Sec. 3. The space-time discretization is presented in Sec. 4. In Sec. 5, we review an a posteriori error representation with respect to a single goal. In Sec. 6, we detail the anisotropic error estimation technique. Sec. 7 describes the algorithm for goal-oriented, anisotropic hp mesh refinement. The solution of the arising algebraic systems is discussed in Sec. 8. Numerical examples are presented in Sec. 9, including a fully time-dependent 3D test case. Finally, Sec. 10 summarizes the results and outlines directions for future research.

2 Mathematical Problem and Notation

Let $\Omega \subset \mathbb{R}^d$ ($d \in \mathbb{N}$) be a bounded Lipschitz domain, and let the boundary be partitioned as $\partial\Omega = \Gamma_D \cup \Gamma_N$, $\Gamma_D \neq \emptyset$, $\Gamma_D \cap \Gamma_N = \emptyset$. Let $I = (0, T]$ denote the time interval, with final time $T > 0$.

We denote by $H^1(\Omega)$ the Sobolev space of $L^2(\Omega)$ functions whose first derivatives are in $L^2(\Omega)$. Define $H := L^2(\Omega)$, $V := H^1(\Omega)$, and $V_0 := H_0^1(\Omega)$ as the space of H^1 -functions with vanishing trace on the Dirichlet boundary Γ_D . The corresponding adjoint spaces are denoted by V' and V'_0 , respectively. The L^2 -inner product is (\cdot, \cdot) , with the norm $\|\cdot\| := \|\cdot\|_{L^2(\Omega)}$. We introduce the continuous space

$$\mathcal{X} := \{ w \in L^2(I; V_0) : \partial_t w \in L^2(I; V'_0) \}, \quad (1)$$

where $L^2(I; V_0)$ is the Bochner space of V_0 -valued functions as defined in [29].

Convection-Diffusion-Reaction Equation. Convection-diffusion-reaction (CDR) equations are fundamental in modeling a wide range of physical phenomena, including fluid dynamics, chemical reactions, and heat transfer. These equations are characterized by the interaction of convective transport, diffusion, and reactive sources or sinks. In this work we study a time-dependent CDR equation given by

$$\partial_t u - \nabla \cdot (\boldsymbol{\varepsilon} \nabla u) + \mathbf{b} \cdot \nabla u + \alpha u = f(\mathbf{x}, t), \quad \text{in } Q = \Omega \times I, \quad (2a)$$

$$u(\mathbf{x}, t) = g(\mathbf{x}, t), \quad \text{on } \Gamma_D \times I, \quad (2b)$$

$$\boldsymbol{\varepsilon} \nabla u \cdot \mathbf{n} = u_N(\mathbf{x}, t), \quad \text{on } \Gamma_N \times I, \quad (2c)$$

$$u(\mathbf{x}, 0) = u_0(\mathbf{x}), \quad \text{in } \Omega, \quad (2d)$$

where Γ_D and Γ_N denote the Dirichlet and Neumann parts of the boundary $\partial\Omega$, respectively, with $\Gamma_D \cup \Gamma_N = \partial\Omega$ and $\Gamma_D \neq \emptyset$. The unit outward normal vector to the boundary is denoted by \mathbf{n} .

In equation (2), the parameter $\boldsymbol{\varepsilon} \in L^\infty(I; W^{1,\infty}(\Omega)^{d \times d})$ represents a symmetric positive definite diffusion coefficient. The convection field $\mathbf{b} \in L^\infty(I; W^{1,\infty}(\Omega)^d)$ governs the advective transport, while $\alpha \in L^\infty(I; L^\infty(\Omega))$ is a reaction coefficient satisfying $\alpha \geq 0$. The source term $f \in L^2(I; H^{-1}(\Omega))$, initial condition $u_0 \in L^2(\Omega)$, Dirichlet boundary data $g \in L^2(I; H^{\frac{1}{2}}(\Gamma_D))$, and Neumann boundary data $u_N \in L^2(I; H^{-\frac{1}{2}}(\Gamma_N))$ are given. To ensure the well-posedness of problem (2), we assume either (i) $\nabla \cdot \mathbf{b}(\mathbf{x}, t) = 0$ and $\alpha(\mathbf{x}, t) \geq 0$, or (ii) that there exists a constant $c_0 > 0$ such that

$$\alpha(\mathbf{x}, t) - \frac{1}{2} \operatorname{div} \mathbf{b}(\mathbf{x}, t) \geq c_0 \quad \forall (\mathbf{x}, t) \in \overline{\Omega} \times \overline{I}. \quad (3)$$

These conditions are standard in the analysis of convection-diffusion-reaction problems of type (2) and ensure coercivity and stability of the associated variational formulation; see, e.g., [2, 66].

Weak Formulation of the CDR Equation. Under the above conditions, problem (2) admits a unique weak solution $u \in \mathcal{X}$ satisfying the variational formulation

$$A(u)(w) = F(w) \quad \forall w \in \mathcal{X}, \quad (4)$$

where the bilinear form $A : \mathcal{X} \times \mathcal{X} \rightarrow \mathbb{R}$ and the linear form $F : \mathcal{X} \rightarrow \mathbb{R}$ are defined by

$$A(u)(w) := \int_I \{(\partial_t u, w) + a(u)(w)\} dt + (u(0), w(0)), \quad F(w) := \int_I (f, w) dt + (u_0, w(0)), \quad (5)$$

with $(v, w) := \int_\Omega v w \, d\mathbf{x}$ and the bilinear form $a : V \times V \rightarrow \mathbb{R}$ given by

$$a(u)(w) := (\boldsymbol{\varepsilon} \nabla u, \nabla w) + (\mathbf{b} \cdot \nabla u, w) + (\alpha u, w). \quad (6)$$

3 Discrete Spaces

We now introduce the discrete space-time meshes and finite element spaces underlying the DG discretization. Letting $t_0 = 0$ and $t_{N_I} = T$, we split the time interval I into a sequence of N_I disjoint subintervals $I_n = (t_{n-1}, t_n]$, $n = 1, \dots, N_I$ with the time step $\tau_n := t_n - t_{n-1}$. By $\mathcal{T}_\tau = \{0\} \cup I_1 \cup \dots \cup I_{N_I}$ we refer to the time mesh.

For the space discretization, let \mathcal{T}_h be a conforming partition of Ω into open quadrilaterals ($d = 2$) or hexahedrals ($d = 3$). Each element $K \in \mathcal{T}_h$ is mapped from the reference cell $\hat{K} = (-1, 1)^d$ by an isoparametric transformation T_K with $\det(T_K)(\hat{\mathbf{x}}) > 0$ for all $\hat{\mathbf{x}} \in \hat{K}$. We decompose

$$T_K := \mathbf{R}_K \circ S_{c,K} \circ S_{h,K} \circ \mathbf{P}_K, \quad (7)$$

where \mathbf{R}_K is a rotation and translation, $S_{c,K}$ is an anisotropic scaling, $S_{h,K}$ is a shearing, and \mathbf{P}_K is a nonlinear component. To account for anisotropic elements, we relax the standard shape-regularity assumptions and require only uniform boundedness of $S_{h,K}$ and \mathbf{P}_K for all $K \in \mathcal{T}_h$. Let $h_{K,i}$, $i = 1, \dots, d$, denote the element size in coordinate direction i . Define the local anisotropy ratio by

$$\rho_K := \max_{\mathbf{x} \in Q_K} \frac{\lambda_{\max}(\mathbf{x})}{\lambda_{\min}(\mathbf{x})}, \quad (8)$$

where Q_K is the set of quadrature points in K , and λ_{\min} , λ_{\max} are the minimal and maximal eigenvalues of $\nabla T_K(\mathbf{x})$, respectively. An element K is called *anisotropic* if $\rho_K > 1$.

For each element K , let $\mathcal{F}(K)$ be its set of $(d-1)$ -dimensional faces, and let $\mathcal{F}_h = \bigcup_{K \in \mathcal{T}_h} \mathcal{F}(K)$, where $\mathcal{F}_h = \mathcal{F}_h^0 \cup \mathcal{F}_h^b$ is partitioned into the sets of interior faces and boundary faces, respectively. For any interior face F , there are exactly two elements K^+ and K^- sharing F , with outward unit normals \mathbf{n}_F^+ (w.r.t. K^+) and \mathbf{n}_F^- (w.r.t. K^-). If $F \in \mathcal{F}_h^b$, then only one element K touches F , and we denote by \mathbf{n}_F its outward unit normal. The $(d-1)$ -measure of F is $|F|$. We denote the space-time tensor product mesh by $\mathcal{T}_{th} = \mathcal{T}_h \times \mathcal{T}_\tau$.

For a $k \in \mathbb{N}_0 := \mathbb{N} \cup \{0\}$ and Banach space B , we let $\mathbb{P}_k(I_n; B)$ denote the set of all polynomials of degree less than or equal to k on I_n with values in B . As we allow hp anisotropic refinements in time, we define k_n as the polynomial degree on interval I_n , which potentially vary significantly. For a multi index $\mathbf{k} = (k_1, \dots, k_{N_I}) \in \mathbb{N}_0^{N_I}$ we define the space of semi-discrete L^2 in time functions as

$$\mathcal{X}_\tau^{\mathbf{k}}(V_0) := \left\{ w_\tau \in L^2(I; V_0) : w_\tau|_{I_n} \in \mathbb{P}_{k_n}(I_n; V_0), w_\tau(0) \in H, \forall n \in \{1, \dots, N_I\} \right\}. \quad (9)$$

3.1 Anisotropic Polynomial Degrees in Space

We define the anisotropic polynomial degree vector on each element $K \in \mathcal{T}_h$ by

$$\mathbf{p}_K = (p_{K,1}, \dots, p_{K,d}) \quad \text{with} \quad p_{K,i} \in \mathbb{N}_0.$$

Definition 3.1 (p -Anisotropic Finite Element). *Let $(p_1, \dots, p_d) \in \mathbb{N}_0^d$ be a multi-index. Then, the anisotropic polynomial space on the reference element $\hat{K} = (-1, 1)^d$ is defined as*

$$\hat{\mathbb{Q}}_{p_1, \dots, p_d}(\hat{K}) := \bigotimes_{i=1}^d \mathbb{P}_{p_i}([-1, 1]),$$

where $\mathbb{P}_p([-1, 1])$ denotes the space of univariate polynomials of degree at most p .

The degrees of freedom (DoFs) are associated with Gauss-Lobatto nodes on each reference element \hat{K} , and the total number of DoFs per element is

$$N_K^{p_1, \dots, p_d} = \prod_{i=1}^d (p_{K,i} + 1).$$

This construction generalizes the isotropic case: for $p_1 = \dots = p_d := p$, we recover the standard space $\hat{\mathbb{Q}}_p(\hat{K})$. The corresponding local finite element space on K consists of tensor-product polynomials:

$$\mathbb{Q}_{p_K}(K) := \bigotimes_{i=1}^d \mathbb{P}_{p_{K,i}}([-1, 1]) \circ T_K^{-1},$$

where T_K is the isoparametric mapping of degree $\max_{i \in \{1, \dots, d\}} p_{K,i}$.

Definition 3.2 (Global p -Anisotropic Finite Element Spaces). *We denote the global finite element space with p -anisotropic elements as defined in Def. 3.1 by*

$$\mathcal{V}_h^{\mathbf{p}} := \{v_h \in L^2(\bar{\Omega}) : v_h|_K \in \mathbb{Q}_{p_K}(K) \forall K \in \mathcal{T}_h\}, \quad p_K = (p_{K,1}, \dots, p_{K,d}), \quad (10)$$

where $\mathbf{p} := (p_K)_{K \in \mathcal{T}_h}$, i.e. the vector of elementwise anisotropic polynomial degrees. Further, for a fixed \mathbf{p} in (10) and $k \in \mathbb{N}$ we introduce the higher-order space

$$\mathcal{V}_h^{\mathbf{p}+\mathbf{k}} := \{v_h \in L^2(\bar{\Omega}) : v_h|_K \in \mathbb{Q}_{p_K+k}(K) \forall K \in \mathcal{T}_h\}, \quad p_K + k := (p_{K,1} + k, \dots, p_{K,d} + k), \quad (11)$$

For the directional error estimation, we also need spaces for restrictions in the i -th spatial direction. For the same \mathbf{p} considered above, we define these spaces as

$$\mathcal{V}_h^{\mathbf{p},i} := \{v_h \in L^2(\bar{\Omega}) : v_h|_K \in \mathbb{Q}_{p_{K-e_i}}(K) \forall K \in \mathcal{T}_h\} \quad (12)$$

where e_i is the i -th unit vector in \mathbb{N}_0^d . We further need an analogous variant of $\mathcal{V}_h^{\mathbf{p},i}$ for the higher-order space $\mathcal{V}_h^{\mathbf{p}+\mathbf{k}}$, which we denote by

$$\mathcal{V}_h^{\mathbf{p}+\mathbf{k},i} := \{v_h \in L^2(\bar{\Omega}) : v_h|_K \in \mathbb{Q}_{p_{K+k-ke_i}}(K), \forall K \in \mathcal{T}_h\}, \quad p_K + k - ke_i = (p_{K,1} + k, \dots, p_{K,d} + k) - ke_i. \quad (13)$$

Definition 3.3 (*p*-Anisotropic Discrete Space-Time Function Spaces.). *We define the discrete space-time function space for (10) by the tensor-products*

$$\mathcal{X}_{\tau h}^{k, p} := \mathcal{X}_\tau^k(\mathbb{R}) \otimes \mathcal{V}_h^p = \text{span}\{\xi \otimes \phi : \xi \in \mathcal{X}_\tau^k(\mathbb{R}), \phi \in \mathcal{V}_h^p\}, \quad (14)$$

where $\xi \otimes \phi(x, t) = \phi(x)\xi(t)$. The space-time function spaces based on the spaces (11)–(13) are defined analogously.

Remark 3.4 (Tensor product function spaces). *For the construction of tensor products of Hilbert spaces we refer to [59, Sec. 1.2.3]. We remark that the space $\mathcal{X}_{\tau h}^{k, p}$ is isometric to the Hilbert space*

$$\mathcal{X}_\tau^k(\mathcal{V}_h^p) = \{w_{\tau h} \in L^2(I; \mathcal{V}_h^p) : w_{\tau h}|_{I_n} \in \mathbb{P}_{k_n}(I_n; \mathcal{V}_h^p), w_{\tau h}(0) \in \mathcal{V}_h^p, \forall n \in \{1, \dots, N_I\}\},$$

see [59, Proposition 1.2.28]. Thus, we identify these pairs of spaces with each other throughout this work. Similarly, we identify $\mathbb{P}_{k_n}(I_n; \mathcal{V}_h^p)$ with $\mathbb{P}_{k_n}(I_n; \mathbb{R}) \otimes \mathcal{V}_h^p$.

For $(x, t) \in \Omega \times \overline{I_n}$, we write

$$w_{\tau h}(x, t)|_{I_n} = \sum_{i=1}^{k_n+1} \left(\sum_{j=1}^{N_x} w_{n,j}^i \phi_j(x) \right) \xi_{n,i}(t),$$

where $\{\phi_j\}_{j=1}^{N_x} \subset \mathcal{V}_h^p$ is the nodal basis, $\{\xi_{n,i}\}_{i=1}^{k_n+1} \subset \mathbb{P}_{k_n}(I_n)$ is the $k_n + 1$ -point Lagrange basis on I_n , and $w_{n,j}^i \in \mathbb{R}$ are the corresponding coefficients.

Given an elementwise defined scalar function v , its *jump* across an interior face $F \in \mathcal{F}_h^0$ shared by elements K^+ and K^- is

$$[v]_F = v^+ - v^-, \quad \text{where } v^+ = v(x)|_{F, K^+}, \quad v^- = v(x)|_{F, K^-}.$$

Similarly, the average of an elementwise defined scalar function v across an interior face $F \in \mathcal{F}_h^0$ shared by elements K^+ and K^- is defined as

$$\{v\} = \frac{1}{2}(v^+ + v^-).$$

Here $v|_{F, K^+}$ means “the trace of v on F as viewed from the element K^+ ”, and similarly for $v|_{F, K^-}$. On a boundary face $F \in \mathcal{F}_h^b$, one typically sets $[v]_F = \{v\}_F = v|_F$, since there is only a single trace on that boundary face.

Throughout this paper, the symbol C denotes a generic positive constant. Its value may change from one occurrence to another and is independent of the mesh size h and other discretization parameters.

3.2 Anisotropic Polynomial Degrees in Time

For hp anisotropic refinements in time we define the temporal basis functions and corresponding temporal matrices. We discretize in time using a discontinuous Galerkin method $\text{DG}(k)$, $k \geq 0$, with trial and test spaces $\mathcal{X}_\tau^k(V_0)$ (cf. (9)). This allows discontinuities across subinterval boundaries and decouples the system at interval endpoints. This enables a piecewise solution with temporal basis functions supported on each subinterval I_n .

Let $\{\hat{\xi}_i\}_{i=1}^{k_n+1} \subset \mathbb{P}_{k_n}(\hat{I}, \mathbb{R})$, $\hat{I} := [-1, 1]$ denote the Lagrangian basis $\mathbb{P}_{k_n}(\hat{I}, \mathbb{R})$ w. r. t. the integration points of the $k_n + 1$ point Gauss-Radau quadrature including the right endpoint. Further, denote by $\mathbb{P}_{k_n}(I_n, \mathbb{R})$ the mapped polynomial space from \hat{I} to I_n with the mapped basis $\{\xi_i\}_{i=1}^{k_n+1}$.

Time Discretization Matrices The matrices for the time discretization are given through the weights $\mathbf{M}_\tau^k \in \mathbb{R}^{k+1 \times k+1}$, $\mathbf{A}_\tau^k \in \mathbb{R}^{k+1 \times k+1}$ and $\mathbf{m}_\tau^k \in \mathbb{R}^{k+1}$, with

$$(\mathbf{M}_\tau^k)_{i,j} := \int_{\hat{I}} \hat{\xi}_j(\hat{t}) \hat{\xi}_i(\hat{t}) d\hat{t}, \quad (\mathbf{A}_\tau^k)_{i,j} := \int_{\hat{I}} \hat{\xi}'_j(\hat{t}) \hat{\xi}_i(\hat{t}) d\hat{t} + \hat{\xi}_j(0) \hat{\xi}_i(0), \quad (\mathbf{m}_\tau^k)_i := \hat{\xi}_i(0), \quad (15)$$

for $i, j = 1, \dots, k + 1$.

4 Space-Time Finite Element Discretization

We now introduce the space-time finite element discretization of the weak formulation (4), based on the discrete spaces from the previous section, which will be used within the DWR framework. In time, we employ DG(k) with slabwise polynomial degrees k_n ; in space, we use p -anisotropic tensor-product elements on quadrilateral/hexahedral meshes. We define the discrete variational form, and the resulting local and global algebraic systems. This prepares the discrete adjoint (by transposition) and the anisotropic error estimator.

Discrete Space-Time Variational Formulation. Given the hp -anisotropic space-time finite element space $\mathcal{X}_{\tau h}^{k,p}$, we formulate the discrete space-time variational problem for the CDR equation. First, we define the spatial DG bilinear form $a_s^Y(\cdot, \cdot)$ by

$$\begin{aligned} a_s^Y(u, w) := & \sum_{K \in \mathcal{T}_h} \left((\boldsymbol{\varepsilon} \nabla u, \nabla w)_K - (u, \mathbf{b} \cdot \nabla w)_K + (\alpha u, w)_K \right) \\ & + \sum_{F \in \mathcal{F}_h^0} \left(-(\boldsymbol{\varepsilon} \{ \nabla u \} \cdot \mathbf{n}_F, [w])_F - ([u], \boldsymbol{\varepsilon} \{ \nabla w \} \cdot \mathbf{n}_F)_F \right. \\ & \quad \left. + \left(\gamma_F \|\boldsymbol{\varepsilon}\|_{L^\infty(F)} + \frac{|\mathbf{b} \cdot \mathbf{n}_F|}{2} \right) ([u], [w])_F + (\mathbf{b} \cdot \mathbf{n}_F \{ u \}, [w])_F \right) \\ & + \sum_{F \in \mathcal{F}_h^b} \left(-(\boldsymbol{\varepsilon} \nabla u \cdot \mathbf{n}_F, w)_F - (u, \boldsymbol{\varepsilon} \nabla w \cdot \mathbf{n}_F)_F + \left(\gamma_F \|\boldsymbol{\varepsilon}\|_{L^\infty(F)} + (\mathbf{b} \cdot \mathbf{n}_F)^+ \right) (u, w)_F \right). \end{aligned} \quad (16)$$

Here, $\gamma_F > 0$ is the penalty parameter we define later. We use the standard notation that $(\cdot, \cdot)_K$ denotes the L^2 -inner product on an element K , with $(\cdot, \cdot)_F$ defined analogously on a face F . Moreover, $(\mathbf{b} \cdot \mathbf{n}_F)^+ = \max(\mathbf{b} \cdot \mathbf{n}_F, 0)$ denotes the positive part of the convective normal flux. Now, we can introduce the space-time discrete variational formulation.

Problem 4.1 (Space-Time Discrete variational form of anisotropic hp -DG for CDR). *Find $u_{\tau h} \in \mathcal{X}_{\tau h}^{k,p}$ such that for all $w_{\tau h} \in \mathcal{X}_{\tau h}^{k,p}$*

$$A_{\tau h}(u_{\tau h}, w_{\tau h}) = F_{\tau h}(w_{\tau h}), \quad (17)$$

where the bilinear form splits into temporal and spatial parts as

$$\begin{aligned} A_{\tau h}(u_{\tau h}, w_{\tau h}) := & \sum_{n=1}^{N_I} \int_{I_n} \left((\partial_t u_{\tau h}, w_{\tau h}) + a_s^Y(u_{\tau h}, w_{\tau h}) \right) dt \\ & + \sum_{n=1}^{N_I-1} \left(([u_{\tau h}]_n, w_{\tau h}(t_n^+)) + ((u_{\tau h}(0^+), w_{\tau h}(0^+)) \right), \end{aligned} \quad (18)$$

and the linear form is given by

$$\begin{aligned} F_{\tau h}(w_{\tau h}) := & \sum_{n=1}^{N_I} \int_{I_n} (f, w_{\tau h}) dt + (u_0, w_{\tau h}(0^+)) \\ & + \sum_{n=1}^{N_I} \int_{I_n} \sum_{F \in \mathcal{F}_h^b} \left(\left(\frac{\gamma \boldsymbol{\varepsilon}}{h_F} + (\mathbf{b} \cdot \mathbf{n}_F)^+ \right) (g, w_{\tau h})_F - (u_N, w_{\tau h})_F \right) dt. \end{aligned} \quad (19)$$

All integrals are taken over space and time, and the jumps $[u_{\tau h}]_n$ and traces $u_{\tau h}(0^+)$ are understood with respect to the DG-in-time discretization. We derive the local and global algebraic systems resulting

from the anisotropic hp -DG discretization of the CDR equations (18). To this end, we define the spatial mass matrix \mathbf{M}_h and stiffness matrix \mathbf{A}_h associated with (16) by

$$\mathbf{M}_h := ((\phi_j, \phi_i))_{i,j=1}^{N_x}, \quad \mathbf{A}_h := (a_s^Y(\phi_j, \phi_i))_{i,j=1}^{N_x},$$

where $\{\phi_i\}_{i=1}^{N_x}$ and $\{\phi_j\}_{j=1}^{N_x} \subset \mathcal{V}_h^p$ denotes a nodal Lagrangian basis of \mathcal{V}_h^p .

Penalty parameter scaling. For robustness on anisotropic hp -meshes we choose the symmetric interior-penalty parameter on a face F shared by K^+ and K^- as

$$\gamma_F = C_{\text{pen}} \frac{1}{2} \left(\frac{p_{K^+,i}(p_{K^+,i} + 1)}{h_F^{K^+}} + \frac{p_{K^-,i}(p_{K^-,i} + 1)}{h_F^{K^-}} \right),$$

with γ_F halved on boundary faces (only one neighbor). Here, h_F^K denotes the directional mesh size of K normal to F and, for $K \in \{K^+, K^-\}$, p_F^K is a representative polynomial degree

$$p_F^K := \max \left\{ 1, \frac{1}{d-1} \sum_{\substack{i=1 \\ i \neq i_F}}^d p_{K,i} \right\},$$

where $i_F \in \{1, \dots, d\}$ is the index of the coordinate direction normal to F . This scaling is similar to the ones proposed in [42, 43] and aligns with anisotropic SIP theory and ensures stability uniformly in h , p , and moderate anisotropy.

Local Algebraic Problem. Upon numerical integration of the discrete variational formulation in Prob. 4.1, we obtain local algebraic systems on each interval I_n . We define the right-hand side vector $\mathbf{F}_n \in \mathbb{R}^{(k_n+1)N_x}$ as

$$\mathbf{F}_n = (f_n^1, \dots, f_n^{k_n+1})^\top,$$

with components given by

$$(f_n^i)_j = \int_{I_n} \left((f, \phi_j \xi_{n,i}) - (\varepsilon \nabla(\phi_j \xi_{n,i}) \cdot \mathbf{n}, g)_{\Gamma_D} - \frac{\gamma}{h_F} (g, \phi_j \xi_{n,i})_{\Gamma_D} \right) dt.$$

Problem 4.2 (Local Algebraic System Anisotropic hp -DG for CDR). *Find $\mathbf{u}_n = (\mathbf{u}_n^1, \dots, \mathbf{u}_n^{k_n+1})^\top$, with $\mathbf{u}_n^i \in \mathbb{R}^{N_x}$, such that*

$$(\tau_n \mathbf{M}_\tau^{k_n} \otimes \mathbf{A}_h + \mathbf{A}_\tau^{k_n} \otimes \mathbf{M}_h) \mathbf{u}_n = \mathbf{F}_n + \mathbf{m}_\tau^{k_n} \otimes \mathbf{M}_h \mathbf{u}_{n-1}^{k_{n-1}+1},$$

with given initial vector $\mathbf{u}_0^{k_0+1}$.

Global Algebraic Problem For a straightforward derivation of the adjoint problem, we construct the global algebraic system for the full time interval I . Define the coupling matrix $\mathbf{B}_n := \mathbf{e}_{k_n+1}^\top \otimes \mathbf{m}_\tau^{k_n} \otimes \mathbf{M}_h$, which corresponds to the temporal jumps. The global algebraic system is then represented as follows.

Problem 4.3 (Global Algebraic System Anisotropic hp -DG for CDR). *Find $(\mathbf{u}_1, \dots, \mathbf{u}_{N_I})^\top$ solving*

$$\begin{pmatrix} S_1 & & & \\ -B_2 & S_2 & & \\ & \ddots & \ddots & \\ & & -B_{N_I} & S_{N_I} \end{pmatrix} \begin{pmatrix} \mathbf{u}_1 \\ \mathbf{u}_2 \\ \vdots \\ \mathbf{u}_{N_I} \end{pmatrix} = \begin{pmatrix} F_1 + \mathbf{m}_\tau^{k_1} \otimes \mathbf{M}_h \mathbf{u}_0^{k_0+1} \\ F_2 \\ \vdots \\ F_{N_I} \end{pmatrix},$$

with block matrices defined as $S_n = \tau_n \mathbf{M}_\tau^{k_n} \otimes \mathbf{A}_h + \mathbf{A}_\tau^{k_n} \otimes \mathbf{M}_h$.

We interpret the time marching scheme as forward substitution in the global system given in Prob. 4.3. This facilitates a straightforward derivation of the global adjoint problem.

Adjoint Algebraic System We now derive the corresponding adjoint system from the global formulation by transposing the global system in Prob. 4.3. We describe this on the discrete level: Based on the global slabwise DG bilinear form (18) in Prob. 4.1, we define the *adjoint variational problem* by the formal Hilbert adjoint

$$A^*(z_{\tau h}, v_{\tau h}) := A(v_{\tau h}, z_{\tau h}), \quad v_{\tau h}, z_{\tau h} \in \mathcal{X}_{\tau h}^{k, p+1}. \quad (20)$$

In particular, we do *not* integrate by parts in space or time. Therefore, the convection direction and temporal orientation are not reversed. Then, the adjoint discretization is, by design, the transpose of the global primal algebraic system in Prob. 4.3. This yields an exact discrete-adjoint pairing for DWR.

For the implementation of the DWR approach, we define the discrete representation of the target functional $J(u)$ on each interval I_n analogously to the right-hand side as

$$(j_n^i)_k = \int_{I_n} (j, \phi_k \xi_{n,i}) \, dt,$$

leading to the global vector $J_n = (j_n^1, \dots, j_n^{k_n+1})^\top$. In the implementation we also support $J(u)$ to be space-time point evaluations. For brevity, we only consider goal functionals that can be evaluated as space-time integrals.

Problem 4.4 (Global Adjoint System Anisotropic hp -DG for CDR). *Let S_n, B_n , and the right-hand side blocks be as in the primal global system of Prob. 4.3. The discrete adjoint unknowns are the vectors $z_n \in \mathbb{R}^{(k_n+1)N_x}$, and the global adjoint system is defined by transposing the primal system:*

$$\begin{pmatrix} S_1^\top & -B_2^\top & & \\ & S_2^\top & -B_3^\top & \\ & & \ddots & \ddots \\ & & & S_{N_I}^\top \end{pmatrix} \begin{pmatrix} z_1 \\ z_2 \\ \vdots \\ z_{N_I} \end{pmatrix} = \begin{pmatrix} J_1 \\ J_2 \\ \vdots \\ J_{N_I} \end{pmatrix},$$

with J_n the goal load on I_n .

The transpose of the global primal system in Prob. 4.3 yields a lower-triangular system. Consequently, the adjoint is solved by backward substitution. The per-slab adjoint system stated below is the corresponding block row of the transposed global system. At each step of the backward substitution, we solve a local slab problem. This mirrors the primal solve, but it is not a time-marching scheme since the time derivative acts on the test function.

Problem 4.5 (Local Adjoint System Anisotropic hp -DG for CDR). *On interval I_n , solve*

$$(\tau_n(M_\tau^{k_n})^\top \otimes A_h + (A_\tau^{k_n})^\top \otimes M_h)z_n = (M_\tau^{k_n})^\top \otimes M_h j_n + e_{k_n+1} \otimes ((M_\tau^{k_n})^\top \otimes M_h)z_{n+1},$$

with $z_{N_I+1} := 0$.

5 A Posteriori Error Representation

In this section, we present a goal-oriented a posteriori error representation based on the Dual Weighted Residual (DWR) method for the space-time DG discretizations considered here. The error is measured with respect to a user-chosen goal functional $J \in C^3(\mathcal{X}, \mathbb{R})$ of the form

$$J(u) = \int_0^T J_t(u(t)) \, dt + J_T(u(T)), \quad (21)$$

where J_t and J_T are three-times continuously differentiable functionals; see, e.g., [21, Ch. 4]. We state the main error representation adapted to our setting and refer to [21, Ch. 4] for a detailed derivation for CDR equations.

For the DWR framework we introduce Lagrangians on the continuous, semi-discrete and fully discrete levels. With $A(\cdot)(\cdot)$ and $F(\cdot)$ as in the weak formulation (5), (19), and with $A_\tau(\cdot, \cdot)$ and $F_\tau(\cdot)$ denoting their time-semi-discrete counterparts, and $A_{\tau h}(\cdot)(\cdot)$ the fully discrete bilinear form of (18), we define

$$\mathcal{L}(u, z) := J(u) + F(z) - A(u)(z), \quad (22a)$$

$$\mathcal{L}_\tau(u_\tau, z_\tau) := J(u_\tau) + F_\tau(z_\tau) - A_\tau(u_\tau)(z_\tau), \quad (22b)$$

$$\mathcal{L}_{\tau h}(u_{\tau h}, z_{\tau h}) := J(u_{\tau h}) + F_{\tau h}(z_{\tau h}) - A_{\tau h}(u_{\tau h})(z_{\tau h}). \quad (22c)$$

Here, (u, z) , (u_τ, z_τ) , and $(u_{\tau h}, z_{\tau h})$ are primal/adjoint pairs at the continuous, time-semi-discrete, and fully discrete levels, respectively. Directional (Gâteaux) derivatives of the Lagrangians with respect to the second argument yield the primal problems on each level, while derivatives with respect to the first argument yield the corresponding adjoint problems; see also [19]. This representation motivates the discretization choices in Sec. 4 and, in particular, the discrete adjoint obtained by transposition of the global primal system (Prob. 4.3), see Sec. 4.4.

We further define the time-semi-discrete primal and adjoint residuals by

$$\rho_\tau(u)(\varphi) := \mathcal{L}'_{\tau,z}(u, z)(\varphi) = F_\tau(\varphi) - A_\tau(u)(\varphi), \quad (23a)$$

$$\rho_\tau^*(u, z)(\varphi) := \mathcal{L}'_{\tau,u}(u, z)(\varphi) = J'(u)(\varphi) - A'_\tau(u)(\varphi, z). \quad (23b)$$

Here $A_\tau : \mathcal{X}_\tau^k(V_0) \times \mathcal{X}_\tau^k(V_0) \rightarrow \mathbb{R}$ denotes the time-semi-discrete DG bilinear form obtained by applying DG in time to the weak form (5) (including slab-interface jump terms). $A_{\tau h} : \mathcal{X}_{\tau h}^{k,p} \times \mathcal{X}_{\tau h}^{k,p} \rightarrow \mathbb{R}$ and $F_{\tau h} : \mathcal{X}_{\tau h}^{k,p} \rightarrow \mathbb{R}$ are the the fully discrete forms. For the error representation, it suffices that $(u_{\tau h}, z_{\tau h})$ satisfies the discrete stationarity conditions $\mathcal{L}'_{\tau h}(u_{\tau h}, z_{\tau h}) = 0$; the concrete assembly of $A_{\tau h}$ and $F_{\tau h}$ is detailed later in Sec. 4.

Theorem 5.1 (Goal-oriented error representation). *Let (u, z) , (u_τ, z_τ) , and $(u_{\tau h}, z_{\tau h})$ be stationary points of \mathcal{L} , \mathcal{L}_τ , and $\mathcal{L}_{\tau h}$, respectively. Then, for arbitrary $(\tilde{u}_\tau, \tilde{z}_\tau)$ in the time-semi-discrete space and $(\tilde{u}_{\tau h}, \tilde{z}_{\tau h})$ in the fully discrete space, the goal-error admits the representations*

$$J(u) - J(u_\tau) = \frac{1}{2} \rho_\tau(u_\tau)(z - \tilde{z}_\tau) + \frac{1}{2} \rho_\tau^*(u_\tau, z_\tau)(u - \tilde{u}_\tau) + \mathcal{R}_\tau, \quad (24a)$$

$$J(u_\tau) - J(u_{\tau h}) = \frac{1}{2} \rho_\tau(u_{\tau h})(z_\tau - \tilde{z}_{\tau h}) + \frac{1}{2} \rho_\tau^*(u_{\tau h}, z_{\tau h})(u_\tau - \tilde{u}_{\tau h}) + \mathcal{R}_h, \quad (24b)$$

where \mathcal{R}_τ and \mathcal{R}_h are higher-order remainders with respect to $(u - u_\tau, z - z_\tau)$ and $(u_\tau - u_{\tau h}, z_\tau - z_{\tau h})$, respectively.

The choices of $(\tilde{u}_\tau, \tilde{z}_\tau)$ and $(\tilde{u}_{\tau h}, \tilde{z}_{\tau h})$ are free and will be instantiated later to obtain temporally and directionally split estimators. In particular, we will use temporal enrichments via lifting and anisotropic spatial restrictions to separate the goal error into temporal and directional spatial parts suitable for anisotropic hp marking.

6 Anisotropic Error Estimation

Building on the error representation (Sec. 5) and the space-time discretization (Sec. 4), we use temporal enrichment and anisotropic spatial restriction to obtain a directional split of the goal error. The resulting error estimators drive the anisotropic hp marking strategy.

We proceed as follows. First, we define anisotropic restriction operators in space and a temporal enrichment by lifting (Sec. 6.1). Next, we connect enrichment and restriction to the DWR representation to obtain temporally and directionally split indicators. These indicators control the anisotropic hp marking strategy described in Sec. 7.

6.1 Anisotropic Restriction Operations

In this section, we use an anisotropic broken L^2 -projection into a directionally restricted finite element space as restriction operator.

Definition 6.1 (The restriction). *Let $v_h \in \mathcal{V}_h^{p+k}$ as in (11). The local restriction operator $R_h^{p_k,k} : \mathbb{Q}_{p_k+k}(K) \rightarrow \mathbb{Q}_{p_k}(K)$ is the local L^2 -projection, i.e., $R_h^{p_k,k} v_h \in \mathbb{Q}_{p_k}(K)$ solves*

$$\int_K (R_h^{p_k,k} v_h) \phi_h \, dx = \int_K v_h \phi_h \, dx \quad \forall \phi_h \in \mathbb{Q}_{p_k}(K), \quad (25)$$

for a fixed $K \in \mathcal{T}_h$. The global restriction operator $R_h^{p,k} : \mathcal{V}_h^{p+k} \rightarrow \mathcal{V}_h^p$ is realized elementwise using the broken L^2 -projection, i.e., $R_h^{p,k} v_h \in \mathcal{V}_h^p$ solves

$$\int_K (R_h^{p,k} v_h) \phi_h \, dx = \int_K v_h \phi_h \, dx \quad \forall \phi_h \in \mathcal{V}_h^p, \forall K \in \mathcal{T}_h. \quad (26)$$

Definition 6.2 (The directional restriction). *For a fixed $k \in \mathbb{N}$ and $i \in \{1, \dots, d\}$, let $v_h \in \mathcal{V}_h^{p+k}$ (cf. (13)). The local directional restriction operator $R_{h,i}^{p_k,k} : \mathbb{Q}_{p_k+k}(K) \rightarrow \mathbb{Q}_{p_k+k-ke_i}(K)$ (cf. (13)) is the local L^2 -projection, i.e., $R_{h,i}^{p_k,k} v_h \in \mathbb{Q}_{p_k+k-ke_i}(K)$ solves*

$$\int_K (R_{h,i}^{p_k,k} v_h) \phi_h \, dx = \int_K v_h \phi_h \, dx \quad \forall \phi_h \in \mathbb{Q}_{p_k+k-ke_i}(K).$$

The global directional restriction operator $R_{h,i}^{p,k} : \mathcal{V}_h^{p+k} \rightarrow \mathcal{V}_h^{p+k,i}$ is realized elementwise by the broken L^2 -projection, i.e., $R_{h,i}^{p,k} v_h \in \mathcal{V}_h^{p+k,i}$ satisfies

$$\int_K (R_{h,i}^{p,k} v_h) \phi_h \, dx = \int_K v_h \phi_h \, dx \quad \forall \phi_h \in \mathcal{V}_h^{p+k,i}, \forall K \in \mathcal{T}_h.$$

Based on Definitions 6.1 and 6.2, we introduce the isotropic error operator as the remainder obtained by comparing the isotropic restriction with the family of directional restrictions.

Definition 6.3 (Isotropic Error Part). *Identifying \mathcal{V}_h^p and $\mathcal{V}_h^{p+k,i}$ with subspaces of \mathcal{V}_h^{p+k} via the canonical injection, we define*

$$\mathbb{E}^{p+k} := (d-1)I + R_h^{p,k} - \sum_{i=1}^d R_{h,i}^{p,k}.$$

The localized version \mathbb{E}^{p_k+k} is given by

$$\mathbb{E}^{p_k+k} := (d-1)I + R_h^{p_k,k} - \sum_{i=1}^d R_{h,i}^{p_k,k}.$$

Lemma 6.4. *For $k \in \mathbb{N} \cup \{0\}$, it holds*

$$\int_{-1}^1 (1-x^2)^k \, dx = B\left(\frac{1}{2}, k+1\right) = \frac{\sqrt{\pi}\Gamma(k+1)}{\Gamma(k+\frac{3}{2})} = \frac{2^{2k}(k!)^2}{(2k+1)!}, \quad (27)$$

where B is the beta function and Γ is the gamma function.

Proof. It holds

$$\int_{-1}^1 (1-x^2)^k \, dx = 2 \int_0^1 (1-x^2)^k \, dx = \int_0^1 t^{-\frac{1}{2}}(1-t)^k \, dt = B\left(\frac{1}{2}, k+1\right). \quad (28)$$

The other equations follows from the properties of the beta function B , the gamma function Γ and $\Gamma\left(\frac{1}{2}\right) = \sqrt{\pi}$. \square

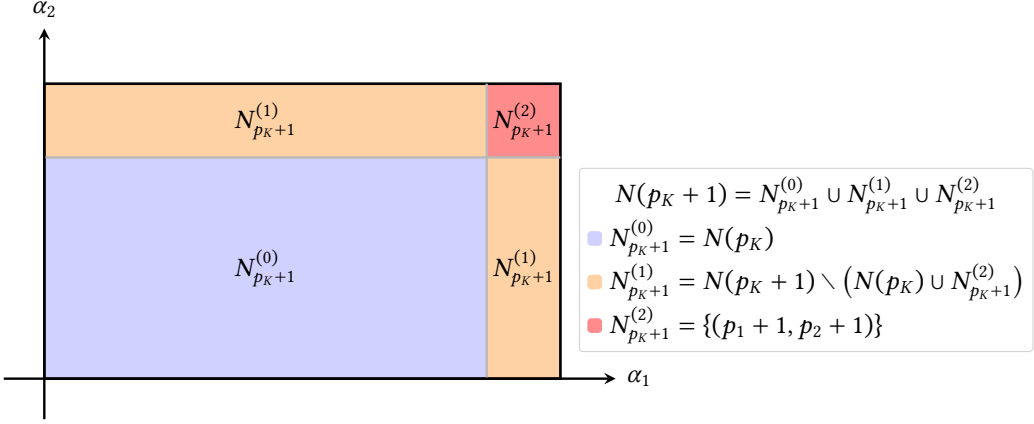


Figure 1: Visualization of the sets $N_{p_K+1}^{(k)}$ for $d = 2$. The union of all sets is $N(p_K + 1)$.

Theorem 6.5. Let $K = \bigotimes_{i=1}^d (0, h_i)$ and let $p_K := (p_1, \dots, p_d)$. Then, for the isotropic error $\|\mathbb{E}^{p+1} v_h\|_{L^2(K)}$, it holds

$$\|\mathbb{E}^{p+1} v_h\|_{L^2(K)} \leq \max_{i,j \in \{1, \dots, d\}, i \neq j} C_{i,j} \|\partial_{x_i}^{p_i+1} \partial_{x_j}^{p_j+1} v_h(x)\|_{L^2(K)} h_i^{p_i+1} h_j^{p_j+1}, \quad (29)$$

with $v_h \in \mathcal{V}_h^{p+1}$ and

$$C_{i,j}^2 := \frac{d^2(d-1)^2(2d-1)}{48(2p_i+2)!(2p_j+2)!2^{(2p_i+2)+(2p_j+2)}} B\left(\frac{1}{2}, p_i+2\right) B\left(\frac{1}{2}, p_j+2\right).$$

Proof. First, let

$$N(p_K) := \{\alpha \in \mathbb{N}_0^d : \alpha_i \leq p_i \forall i\}, \quad N(p_K + 1) := \{\alpha \in \mathbb{N}_0^d : \alpha_i \leq p_i + 1 \forall i\},$$

and for $k \in \{0, \dots, d\}$ define $N_{p_K+1}^{(k)} := \{\alpha \in N(p_K + 1) : |\{i : \alpha_i = p_i + 1\}| = k\}$. See Fig. 1 for a visualization of these multiindex sets for $d = 2$. Furthermore, let $T_K : \hat{K} \rightarrow K$ be implicitly defined via

$$[T_K^{-1}(x)]_i = \hat{x}_i := \frac{2x_i - h_i}{h_i}. \quad (30)$$

For $v_h \in \mathcal{V}_h^{p+1}$ and an arbitrary but fixed $K \in \mathcal{T}_h$, we define $\hat{v} := v_{h,K} \circ T_K$. Furthermore, let $L_\alpha : \hat{K} \rightarrow \mathbb{R}$ be the tensor-product Legendre-Polynomial of degree $\alpha \in \mathbb{N}^d$; see [70]. Since \hat{v} is a multivariate polynomial of degree $p_K + 1 = (p_1 + 1, \dots, p_d + 1)$, the polynomial \hat{v} can be written as

$$\hat{v}(\hat{x}) = \sum_{\alpha \in N(p_K+1)} b_\alpha L_\alpha(\hat{x}) \quad \text{with} \quad b_\alpha := \int_{\hat{K}} \hat{v}(\hat{y}) L_\alpha(\hat{y}) d\hat{y} \prod_{i=1}^d \frac{2\alpha_i + 1}{2}, \quad (31)$$

where $\alpha := (\alpha_1, \dots, \alpha_d) \in \mathbb{N}_0^d$ and $L_\alpha(\hat{x}) := \prod_{i=1}^d L_{\alpha_i}(\hat{x}_i)$. With a slight abuse of notation, we denote by $R_h^{p_K}$ and $R_{h,i}^{p_K}$ also the corresponding projectors on \hat{K} obtained by pullback with T_K . Then, one can show that

$$R_h^{p_K} \hat{v}(\hat{x}) := \sum_{\alpha \in N(p_K)} b_\alpha L_\alpha(\hat{x}), \quad (32)$$

and

$$R_{h,i}^{p_K} \hat{v}(\hat{x}) := \sum_{\alpha \in N(p_K+1-e_i)} b_\alpha L_\alpha(\hat{x}). \quad (33)$$

From the definition of \mathbb{E}^{p+1} we know that

$$\mathbb{E}^{p_K+1} := (d-1)I + R_h^{p_K} - \sum_{i=1}^d R_{h,i}^{p_K}. \quad (34)$$

Therefore, we get that

$$\begin{aligned} \mathbb{E}^{p+1}\hat{v}(\hat{x}) &:= (d-1) \sum_{\alpha \in N(p_K+1)} b_\alpha L_\alpha(\hat{x}) + \sum_{\alpha \in N(p_K)} b_\alpha L_\alpha(\hat{x}) - \sum_{i=1}^d \sum_{\alpha \in N(p_K+1-e_i)} b_\alpha L_\alpha(\hat{x}) \\ &= d \sum_{\alpha \in N(p_K+1)} b_\alpha L_\alpha(\hat{x}) \\ &\quad - \sum_{\alpha \in (N(p_K+1) \setminus N(p_K))} b_\alpha L_\alpha(\hat{x}) - \sum_{i=1}^d \sum_{\alpha \in N(p_K+1-e_i)} b_\alpha L_\alpha(\hat{x}) \\ &= \sum_{i=1}^d \sum_{\alpha \in (N(p_K+1) \setminus N(p_K+1-e_i))} b_\alpha L_\alpha(\hat{x}) - \sum_{\alpha \in (N(p_K+1) \setminus N(p_K))} b_\alpha L_\alpha(\hat{x}). \end{aligned} \quad (35)$$

We observe that $N(p_K+1) \setminus N(p_K) = \{\alpha \in N(p_K+1) : \exists i \in \{1, \dots, d\}, \alpha_i = p_i + 1\}$ and $N(p_K+1) \setminus N(p_K+1-e_i) = \{\alpha \in N(p_K+1) : \alpha_i = p_i + 1\}$, see also Fig. 1. Then, we see that

$$\sum_{i=1}^d \sum_{\alpha \in (N(p_K+1) \setminus N(p_K+1-e_i))} b_\alpha L_\alpha(\hat{x}) = \sum_{k=1}^d k \sum_{\alpha \in N_{p_K+1}^{(k)}} b_\alpha L_\alpha(\hat{x}), \quad (36)$$

and

$$\sum_{\alpha \in (N(p_K+1) \setminus N(p_K))} b_\alpha L_\alpha(\hat{x}) = \sum_{k=1}^d \sum_{\alpha \in N_{p_K+1}^{(k)}} b_\alpha L_\alpha(\hat{x}). \quad (37)$$

Using (37) and (36) we can rewrite (35) as

$$\mathbb{E}^{p+1}\hat{v}(\hat{x}) := \sum_{k=1}^d (k-1) \sum_{\alpha \in N_{p_K+1}^{(k)}} b_\alpha L_\alpha(\hat{x}) = \sum_{k=1}^{d-1} k \sum_{\alpha \in N_{p_K+1}^{(k+1)}} b_\alpha L_\alpha(\hat{x}). \quad (38)$$

Let $\hat{x}'_i := (\hat{x}_1, \dots, \hat{x}_{i-1}, \hat{x}_{i+1}, \dots, \hat{x}_d)$. Using [70, Lemma 3.10] and the tensor product property of L_α and \hat{K} we get that for α with $\alpha_i = p_i + 1$

$$\sum_{\substack{\alpha \\ \alpha_i = p_i+1}} b_\alpha^2 \prod_{j=1}^d \frac{2}{2\alpha_j + 1} = \frac{1}{(2p_i+2)!} \int_{\bigotimes_{j=1}^d [-1,1]} \int_{-1}^1 |\partial_{\hat{x}_i}^{p_i+1} \hat{v}(\hat{x})|^2 (1 - \hat{x}_i^2)^k d\hat{x}_i d\hat{x}'_i. \quad (39)$$

In combination with Lemma 6.4 and that $\partial_{\hat{x}_i}^{p_i+1} \hat{v}(\hat{x})$ is constant with respect to \hat{x}_i , it holds

$$\sum_{\substack{\alpha \\ \alpha_i = p_i+1}} b_\alpha^2 \prod_{j=1}^d \frac{2}{2\alpha_j + 1} = \frac{1}{(2p_i+2)!} B\left(\frac{1}{2}, p_i + 2\right) \int_{\bigotimes_{j=1}^d [-1,1]} |\partial_{\hat{x}_i}^{p_i+1} \hat{v}(\hat{x})|^2 d\hat{x}'_i. \quad (40)$$

Finally, we can deduce that

$$\sum_{\substack{\alpha \\ \alpha_i = p_i+1}} b_\alpha^2 \prod_{j=1}^d \frac{2}{2\alpha_j + 1} = \frac{1}{(2p_i+2)!2} B\left(\frac{1}{2}, p_i + 2\right) \int_{\hat{K}} |\partial_{\hat{x}_i}^{p_i+1} \hat{v}(\hat{x})|^2 d\hat{x}. \quad (41)$$

For α where $\alpha_i = p_i + 1$ and $\alpha_j = p_j + 1$, one can show in a similar fashion

$$\sum_{\substack{\alpha \\ \alpha_i = p_i + 1 \\ \alpha_j = p_j + 1}} b_\alpha^2 \prod_{k=1}^d \frac{2}{2\alpha_k + 1} = \frac{1}{(2p_i + 2)!(2p_j + 2)!4} B\left(\frac{1}{2}, p_i + 2\right) B\left(\frac{1}{2}, p_j + 2\right) \int_{\hat{K}} |\partial_{\hat{x}_i}^{p_i+1} \partial_{\hat{x}_j}^{p_j+1} \hat{v}(\hat{x})|^2 d\hat{x}. \quad (42)$$

Finally from [70, (3.3.6)] and (38), we know that

$$\|\mathbb{E}^{\mathbf{p}+1} \hat{v}\|_{L^2(\hat{K})}^2 = \sum_{k=1}^{d-1} k^2 \sum_{\alpha \in N_{p_K+1}^{(k+1)}} b_\alpha^2 \prod_{l=1}^d \frac{2}{\alpha_l + 1}. \quad (43)$$

This concludes that

$$\|\mathbb{E}^{\mathbf{p}+1} \hat{v}\|_{L^2(\hat{K})}^2 \leq \sum_{k=1}^{d-1} k^2 \max_{\substack{i, j \in \{1, \dots, d\} \\ i \neq j}} \tilde{C}_{i,j} \|\partial_{\hat{x}_i}^{p_i+1} \partial_{\hat{x}_j}^{p_j+1} \hat{v}\|_{L^2(\hat{K})}^2, \quad (44)$$

where

$$\tilde{C}_{i,j} := \frac{d(d-1)}{(2p_i + 2)!(2p_j + 2)!8} B\left(\frac{1}{2}, p_i + 2\right) B\left(\frac{1}{2}, p_j + 2\right).$$

Finally, we have

$$\begin{aligned} \|\mathbb{E}^{\mathbf{p}+1} v_h\|_{L^2(K)}^2 &= \|\mathbb{E}^{\mathbf{p}+1} \hat{v}\|_{L^2(\hat{K})}^2 \prod_{i=1}^d \frac{h_i}{2} \\ &\leq \frac{d(d-1)(2d-1)}{6} \max_{\substack{i, j \in \{1, \dots, d\} \\ i \neq j}} \tilde{C}_{i,j} \|\partial_{\hat{x}_i}^{p_i+1} \partial_{\hat{x}_j}^{p_j+1} \hat{v}\|_{L^2(\hat{K})}^2 \prod_{k=1}^d \frac{h_k}{2} \\ &= \frac{d(d-1)(2d-1)}{6} \max_{\substack{i, j \in \{1, \dots, d\} \\ i \neq j}} \tilde{C}_{i,j} \|\partial_{x_i}^{p_i+1} \partial_{x_j}^{p_j+1} v_h\|_{L^2(K)}^2 \left(\frac{h_i}{2}\right)^{2(p_i+1)} \left(\frac{h_j}{2}\right)^{2(p_j+1)} \end{aligned} \quad (45)$$

The proof is completed by taking the square root. \square

Corollary 6.6. *Let $d = 2$, $K = (0, h_1) \times (0, h_2)$ and $p_K := (p_1, p_2)$. Then, for the isotropic error $\|\mathbb{E}^{\mathbf{p}+1} v_h\|_{L^2(K)}$, it holds*

$$\|\mathbb{E}^{\mathbf{p}+1} v_h\|_{L^2(K)} = C_{1,2} \|\partial_{x_1}^{p_1+1} \partial_{x_2}^{p_2+1} v_h(x)\|_{L^2(K)} h_1^{p_1+1} h_2^{p_2+1}, \quad (46)$$

with $v_h \in \mathcal{V}_h^{\mathbf{p}+1}$ and

$$C_{1,2}^2 := \frac{1}{4(2p_1 + 2)!(2p_2 + 2)!2^{(2p_1+2)+(2p_2+2)}} B\left(\frac{1}{2}, p_1 + 2\right) B\left(\frac{1}{2}, p_2 + 2\right).$$

Proof. Follow the same steps as in Theorem 6.5 and verify that the inequalities become equalities. \square

Remark 6.7. *Even though Theorem 6.5 and Corollary 6.6 are proven for hyperrectangles $K = \bigotimes_{i=1}^d (0, h_i)$, the same estimate extends to parallelepipeds, i.e., affine images of the reference cell \hat{K} . More precisely, let $T_K : \hat{K} \rightarrow K$ be an affine bijection of the form $T_K(\hat{x}) = B\hat{x} + b$, with constant Jacobian matrix $B \in \mathbb{R}^{d \times d}$. Then the scaling of derivatives is governed by B^{-1} , and the constants in the above bounds depend on B . Since the Jacobian is constant, the change-of-variables arguments used in the proof carry over verbatim.*

6.2 Spatial and Temporal enrichment

Temporal enrichment via lifting In the hp -adaptive setting we use a local-in-time map that turns a piecewise $DG(k_n)$ function into a continuous function of one higher local degree while preserving the DG nodal values at the right Gauss–Radau points on each slab $I_n = (t_{n-1}, t_n]$. Following the Radau lifting in [38, Sec. 3.2, (3.11)–(3.14)], we construct on every slab the *unique* polynomial $\vartheta_n \in \mathbb{P}_{k_n+1}(I_n)$ that equals 1 at the left endpoint t_{n-1}^+ and vanishes at the $(k_n + 1)$ right-sided Gauss–Radau nodes $\{t_{n,\mu}\}_{\mu=1}^{k_n+1} \subset \overline{I_n}$ (with $t_{n,k_n+1} = t_n$). Subtracting the temporal jump multiplied by ϑ_n cancels the discontinuity while leaving all Radau nodal values intact, and raises the local degree by one; see also the use of L_τ in the DG-in-time formulation in [38, Lem. 3.2].

Definition 6.8 (Lifting-based temporal enrichment). *Let B be a Banach space and $\mathbf{k} = (k_n)_{n=1}^N$. For $w_\tau \in \mathcal{X}_\tau^k(B)$ define $\mathcal{L}_\tau w_\tau \in \mathcal{X}_\tau^{k+1}(B) \cap C^0(\overline{I}; B)$ by*

$$(\mathcal{L}_\tau w_\tau)(t) := w_\tau(t) - [w_\tau]_{n-1} \vartheta_n(t) \quad \text{for } t \in I_n, \quad (\mathcal{L}_\tau w_\tau)(0) := w_\tau(0),$$

where $[w_\tau]_{n-1} := \lim_{t \rightarrow t_{n-1}^+} w_\tau(t) - \lim_{t \rightarrow t_{n-1}^-} w_\tau(t)$ and $\vartheta_n \in \mathbb{P}_{k_n+1}(I_n)$ satisfies

$$\vartheta_n(t_{n-1}^+) = 1, \quad \vartheta_n(t_{n,\mu}) = 0, \quad \mu = 1, \dots, k_n + 1.$$

Remark 6.9 (Properties of the temporal enrichment).

Continuity and interpolation. *On each slab I_n , $(\mathcal{L}_\tau w_\tau)(t_{n-1}^+) = w_\tau(t_{n-1}^-)$ and $(\mathcal{L}_\tau w_\tau)(t_{n,\mu}) = w_\tau(t_{n,\mu})$ for $\mu = 1, \dots, k_n + 1$, hence $\mathcal{L}_\tau w_\tau$ is continuous on \overline{I} and preserves all right Radau values [38, (3.12)–(3.14)].*

Degree elevation. *$(\mathcal{L}_\tau w_\tau)|_{I_n} \in \mathbb{P}_{k_n+1}(I_n; B)$, so the local temporal degree increases by one [38, (3.11)–(3.12)].*

Locality and block structure. *\mathcal{L}_τ acts slabwise and depends only on the jump $[w_\tau]_{n-1}$; globally it is block-diagonal with respect to the slabs [38, Sec. 3.2].*

L^2 -stability. *There exists $C_L \geq 1$, depending only on $\max_n k_n$ and the (reference) Radau nodes, such that*

$$\|\mathcal{L}_\tau v\|_{L^2(I; B)} \leq C_L \|v\|_{L^2(I; B)} \quad \forall v \in \mathcal{X}_\tau^k(B).$$

The constant is independent of h and of the time-step sizes. This follows by scaling of [38, (3.13)] and standard DG jump–trace bounds (see the discussion in [38, Sec. 3.2]).

Lifting on \hat{I} . *On the interval $\hat{I} = (-1, 1)$ the lifting polynomial can be written explicitly as*

$$\hat{\vartheta}(\hat{t}) = \prod_{\mu=1}^{k_n+1} \frac{\hat{t} - \hat{t}_\mu}{-1 - \hat{t}_\mu},$$

where $\{\hat{t}_\mu\}$ are the right Gauss–Radau nodes on \hat{I} (cf. [38, (3.13)]). Mapping $I_n \rightarrow \hat{I}$ yields ϑ_n . The stability follows by scaling.

Spatial enrichment through higher-order solution We realize spatial enrichment by solving the primal and the adjoint problems on the higher-order space \mathcal{V}_h^{p+1} . These enriched solutions are used to build the error estimators.

Definition 6.10 (Spatial enrichment). *Let \mathcal{V}_h^p be the current spatial space (10) and \mathcal{V}_h^{p+1} the space with all local degrees raised by one (11). For a fixed temporal discretization and global bilinear form $A_{\tau h}(\cdot)(\cdot)$ with right-hand side $F_{\tau h}$, the primal enriched solution $u_{\tau h}^{p+1} \in \mathcal{X}_{\tau h}^{k, p+1}$ is defined by*

$$A_{\tau h}(u_{\tau h}^{p+1})(w) = F_{\tau h}(w) \quad \forall w \in \mathcal{X}_{\tau h}^{k, p+1}.$$

For a goal functional J , the adjoint enriched solution $z_{\tau h}^{p+1} \in \mathcal{X}_{\tau h}^{k, p+1}$ solves

$$A_{\tau h}(w)(z_{\tau h}^{p+1}) = J'(u_{\tau h}^{p+1})(w) \quad \forall w \in \mathcal{X}_{\tau h}^{k, p+1}.$$

Connection to anisotropic DWR estimators We use the lifting \mathcal{L}_τ as the concrete temporal enrichment in the time-estimator components; i.e., in the formulas (54a) and (57c) we take $E_\tau^{(k+1)} := \mathcal{L}_\tau$. On the spatial side, all enrichment terms are evaluated with the enriched solutions $u_{\tau h}^{p+1}$ and $z_{\tau h}^{p+1}$ from Def. 6.10. Directional splitting is effected with the directional restrictions $R_{h,i}$, so that differences of the form $v - R_{h,i}v$ isolate the contribution in direction i . This realization yields the temporal indicators η_τ^p , η_τ^{p+1} and the directional spatial indicators $\{\eta_{h,i}^{p+1}\}_{i=1}^d$ and $\{\eta_{h,i}^p\}_{i=1}^d$ used for anisotropic hp marking. Here, $\eta_{h,i}^{p+1}$ is evaluated in the higher-order space of degree $p+1$, and $\eta_{h,i}^p$ denotes the corresponding indicator evaluated after restricting the discrete solution to degree p . This pair enables the definition of a local saturation indicator, which measures how much of the estimated error is already captured on the current space and how much is reduced by p -enrichment.

6.3 Anisotropic Goal Oriented Error Estimation

In this section, we briefly describe the theoretical background of the error estimator.

Theorem 6.11. *Let $u_{\tau h}^p$ be an approximation of the discrete solution and u be the continuous solution. Furthermore let $u_{\tau h}^{p+1}$, $z_{\tau h}^p$, $z_{\tau h}^{p+1}$ and $z_{\tau h}^p$ be arbitrary. Then it holds*

$$J(u) - J(u_{\tau h}^p) = J(u) - J(E_\tau^{(k+1)} u_{\tau h}^{p+1}) + \eta_h^{p+1} + \eta_{h,\approx}^{p+1} + \eta_\tau^{p+1} + \eta_{\tau,\approx}^{p+1}, \quad (47)$$

where

$$\begin{aligned} \eta_h^{p+1} &:= \eta_{\tau h}(u_{\tau h}^p, u_{\tau h}^{p+1}, z_{\tau h}^{p+1}, u_{\tau h}^p, z_{\tau h}^p), \\ \eta_{h,\approx}^{p+1} &:= \eta_{\tau h,\approx}(u_{\tau h}^p, u_{\tau h}^{p+1}, z_{\tau h}^{p+1}, u_{\tau h}^p, z_{\tau h}^p) + \eta_k(u_{\tau h}^p, z_{\tau h}^p) + \eta_R(u_{\tau h}^{p+1}, z_{\tau h}^{p+1}, u_{\tau h}^p, z_{\tau h}^p), \\ \eta_\tau^{p+1} &:= \eta_{\tau h}(u_{\tau h}^{p+1}, E_\tau^{(k+1)} u_{\tau h}^{p+1}, E_\tau^{(k+1)} z_{\tau h}^{p+1}, u_{\tau h}^{p+1}, z_{\tau h}^{p+1}), \\ \eta_{\tau,\approx}^{p+1} &:= \eta_{\tau h,\approx}(u_{\tau h}^{p+1}, E_\tau^{(k+1)} u_{\tau h}^{p+1}, E_\tau^{(k+1)} z_{\tau h}^{p+1}, u_{\tau h}^{p+1}, z_{\tau h}^{p+1}) + \eta_k(u_{\tau h}^{p+1}, z_{\tau h}^{p+1}) \\ &\quad + \eta_R(E_\tau^{(k+1)} u_{\tau h}^{p+1}, E_\tau^{(k+1)} z_{\tau h}^{p+1}, u_{\tau h}^p, z_{\tau h}^p), \end{aligned}$$

and

$$\begin{aligned} \eta_{\tau h}(u, v, z, v_{\tau h}, z_{\tau h}) &:= \frac{1}{2} \rho_\tau(u)(z - z_{\tau h}) + \frac{1}{2} \rho_\tau^*(u, z_{\tau h})(v - v_{\tau h}), \\ \eta_{\tau h,\approx}(u, v, z, v_{\tau h}, z_{\tau h}) &:= \frac{1}{2} \rho_\tau(u)(z + z_{\tau h}) + \frac{1}{2} \rho_\tau^*(u, z)(v - v_{\tau h}), \\ \eta_k(u, z) &:= -\rho_\tau(u)(z), \\ \eta_R(u, z, u_{\tau h}, z_{\tau h}) &:= \int_0^1 \left[J'''(u - s(u - u_{\tau h}))(u - u_{\tau h}, u - u_{\tau h}, u - u_{\tau h}) \right. \\ &\quad \left. - A'''(u - s(u - u_{\tau h}))(u - u_{\tau h}, u - u_{\tau h}, u - u_{\tau h}, z - s(z - z_{\tau h})) \right. \\ &\quad \left. - 3A''(u - s(u - u_{\tau h}))(u - u_{\tau h}, u - u_{\tau h}, z - z_{\tau h}) \right] (s-1) s \, ds. \end{aligned}$$

Proof. Using Thm. 7 of [37] we obtain

$$\begin{aligned}
J(u) - J(u_{\tau h}^p) &= J(u) - J(E_\tau^{(k+1)} u_{\tau h}^{p+1}) + J(E_\tau^{(k+1)} u_{\tau h}^{p+1}) - J(u_{\tau h}^{p+1}) + J(u_{\tau h}^{p+1}) - J(u_{\tau h}^p) \\
&= J(u) - J(E_\tau^{(k+1)} u_{\tau h}^{p+1}) \\
&\quad + \frac{1}{2} \rho_\tau(u_{\tau h}^{p+1}) (E_\tau^{(k+1)} z_{\tau h}^{p+1} - z_{\tau h}^{p+1}) + \frac{1}{2} \rho_\tau^*(u_{\tau h}^{p+1}, z_{\tau h}^{p+1}) (E_\tau^{(k+1)} u_{\tau h}^{p+1} - u_{\tau h}^{p+1}) \\
&\quad - \rho_\tau(u_{\tau h}^{p+1}) (z_{\tau h}^{p+1}) + \frac{1}{2} \rho_\tau(E_\tau^{(k+1)} u_{\tau h}^{p+1}) (E_\tau^{(k+1)} z_{\tau h}^{p+1} + z_{\tau h}^{p+1}) \\
&\quad + \frac{1}{2} \rho_\tau^*(E_\tau^{(k+1)} u_{\tau h}^{p+1}, E_\tau^{(k+1)} z_{\tau h}^{p+1}) (E_\tau^{(k+1)} u_{\tau h}^{p+1} - u_{\tau h}^{p+1}) \\
&\quad + \eta_R(E_\tau^{(k+1)} u_{\tau h}^{p+1}, E_\tau^{(k+1)} z_{\tau h}^{p+1}, u_{\tau h}^{p+1}, z_{\tau h}^{p+1}) \\
&\quad + \frac{1}{2} \rho_\tau(u_{\tau h}^p) (z_{\tau h}^{p+1} - z_{\tau h}^p) + \frac{1}{2} \rho_\tau^*(u_{\tau h}^p, z_{\tau h}^p) (u_{\tau h}^{p+1} - u_{\tau h}^p) - \rho_\tau(u_{\tau h}^p) (z_{\tau h}^p) \\
&\quad + \frac{1}{2} \rho_\tau(u_{\tau h}^{p+1}) (z_{\tau h}^{p+1} + z_{\tau h}^p) + \frac{1}{2} \rho_\tau^*(u_{\tau h}^{p+1}, z_{\tau h}^{p+1}) (u_{\tau h}^{p+1} - u_{\tau h}^p) + \eta_R(u_{\tau h}^{p+1}, z_{\tau h}^{p+1}, u_{\tau h}^p, z_{\tau h}^p) \\
&= J(u) - J(E_\tau^{(k+1)} u_{\tau h}^{p+1}) + \eta_{\tau h}(u_{\tau h}^{p+1}, E_\tau^{(k+1)} u_{\tau h}^{p+1}, E_\tau^{(k+1)} z_{\tau h}^{p+1}, u_{\tau h}^{p+1}, z_{\tau h}^{p+1}) \\
&\quad + \eta_{\tau h, \approx}(u_{\tau h}^{p+1}, E_\tau^{(k+1)} u_{\tau h}^{p+1}, E_\tau^{(k+1)} z_{\tau h}^{p+1}, u_{\tau h}^{p+1}, z_{\tau h}^{p+1}) + \eta_k(u_{\tau h}^{p+1}, z_{\tau h}^{p+1}) \\
&\quad + \eta_R(E_\tau^{(k+1)} u_{\tau h}^{p+1}, E_\tau^{(k+1)} z_{\tau h}^{p+1}, u_{\tau h}^{p+1}, z_{\tau h}^{p+1}) \\
&\quad + \eta_{\tau h}(u_{\tau h}^p, u_{\tau h}^{p+1}, z_{\tau h}^{p+1}, u_{\tau h}^p, z_{\tau h}^p) + \eta_{\tau h, \approx}(u_{\tau h}^p, u_{\tau h}^{p+1}, z_{\tau h}^{p+1}, u_{\tau h}^p, z_{\tau h}^p) \\
&\quad + \eta_k(u_{\tau h}^p, z_{\tau h}^p) + \eta_R(u_{\tau h}^{p+1}, z_{\tau h}^{p+1}, u_{\tau h}^p, z_{\tau h}^p)
\end{aligned}$$

□

Remark 6.12. According to Thm. 6.11, the error $J(u) - J(u_{\tau h}^p)$ can be split into the error $J(u) - J(E_\tau^{(k+1)} u_{\tau h}^{p+1})$ and several error estimator components: η_h^{p+1} , $\eta_{h, \approx}^{p+1}$, η_τ^{p+1} , and $\eta_{\tau, \approx}^{p+1}$. Here, η_h^{p+1} and η_τ^{p+1} correspond to the discretization error in space and time, respectively. Therefore, η_h^{p+1} and η_τ^{p+1} can be used to drive the adaptivity. The components $\eta_{h, \approx}^{p+1}$ and $\eta_{\tau, \approx}^{p+1}$ capture the inaccuracies related to not solving the problem at higher-orders in space and time, as well as the inaccuracies when solving for $u_{\tau h}^p$ and higher-order components. These parts will be neglected for the adaptivity.

Error estimator in practice Let $R_h^p := R_h^{p,1}$ and $R_{h,i}^p := R_{h,i}^{p,1}$. For the error estimator in practice this, we replace $u_{\tau h}^p$ by $R_h^p u_{\tau h}^{p+1}$ and $z_{\tau h}^p$ by $R_h^p z_{\tau h}^{p+1}$. The resulting discretization error estimator η_h^{p+1} is given by

$$\eta_h^{p+1} := \frac{1}{2} \rho_\tau(R_h^p u_{\tau h}^{p+1}) (z_{\tau h}^{p+1} - R_h^p z_{\tau h}^{p+1}) + \frac{1}{2} \rho_\tau^*(R_h^p u_{\tau h}^{p+1}, R_h^p z_{\tau h}^{p+1}) (u_{\tau h}^{p+1} - R_h^p u_{\tau h}^{p+1}) \quad (48)$$

Theorem 6.13. Let η_h^{p+1} be defined as in (48). Then, η_h^{p+1} can be decomposed as follows

$$\eta_h^{p+1} := \left(\sum_{i=1}^d \eta_{h,i}^{p+1} \right) - \eta_{h,\mathbb{E}}^{p+1}. \quad (49)$$

where for $i \in \{1, \dots, d\}$, we define

$$\eta_{h,i}^{p+1} := \frac{1}{2} \rho_\tau(R_h^p u_{\tau h}^{p+1}) (z_{\tau h}^{p+1} - R_{h,i}^{p+1} z_{\tau h}^{p+1}) + \frac{1}{2} \rho_\tau^*(R_h^p u_{\tau h}^{p+1}, R_{h,i}^{p+1} z_{\tau h}^{p+1}) (u_{\tau h}^{p+1} - R_{h,i}^{p+1} u_{\tau h}^{p+1}), \quad (50)$$

and

$$\eta_{h,\mathbb{E}}^{p+1} := \frac{1}{2} \rho_\tau(R_h^p u_{\tau h}^{p+1}) (\mathbb{E}^{p+1} z_{\tau h}^{p+1}) + \frac{1}{2} \rho_\tau^*(R_h^p u_{\tau h}^{p+1}, R_h^p z_{\tau h}^{p+1}) (\mathbb{E}^{p+1} u_{\tau h}^{p+1}). \quad (51)$$

Proof. For η_h^p we follow the idea of to [15]. From the definition of $\mathbb{E}^{p_{K+1}}$ we know

$$\mathbb{E}^{p_{K+1}} := (d-1)I + \mathbf{R}_h^p - \sum_{i=1}^d \mathbf{R}_{h,i}^{p+1}. \quad (52)$$

Subtracting $\mathbb{E}^{p_{K+1}}$ and adding $I - \mathbf{R}_h^p$ yields

$$I - \mathbf{R}_h^p = -\mathbb{E}^{p_{K+1}} + dI - \sum_{i=1}^d \mathbf{R}_{h,i}^{p+1} = -\mathbb{E}^{p_{K+1}} + \sum_{i=1}^d I - \mathbf{R}_{h,i}^{p+1}.$$

The rest follows as in [15] by using the shown identity and the linearity of the parts $u_{\tau h}^{p+1} - \mathbf{R}_h^p u_{\tau h}^{p+1}$ and $z_{\tau h}^{p+1} - \mathbf{R}_h^p z_{\tau h}^{p+1}$ in (48). \square

Theorem 6.14. *Let us assume there exists $\beta \in (0, 1)$ and $\beta_{h,\tau} \in (0, \beta)$ such that*

$$\left| J(u) - J(\mathbf{E}_\tau^{(k+1)} u_{\tau h}^{p+1}) \right| + \left| \eta_{h,\mathbb{E}}^{p+1} + \eta_{h,\approx}^{p+1} + \eta_{\tau,\approx}^{p+1} \right| \leq \beta_{h,\tau} \left| J(u) - J(\mathbf{R}_h^p u_{\tau h}^{p+1}) \right|.$$

Then, it holds that

$$\frac{1}{1 + \beta_{h,\tau}} \left| \eta_\tau^{p+1} + \sum_{i=1}^d \eta_{h,i}^{p+1} \right| \leq \left| J(u) - J(\mathbf{R}_h^p u_{\tau h}^{p+1}) \right| \leq \frac{1}{1 - \beta_{h,\tau}} \left| \eta_\tau^{p+1} + \sum_{i=1}^d \eta_{h,i}^{p+1} \right|. \quad (53)$$

Proof. The proof is analogous to the proof of [34, Theorem 3.9] and [36, Theorem 3.12]. \square

Remark 6.15. *From Theorem 6.5, we know that $\eta_{h,\mathbb{E}}^{p+1}$ is of higher order and is therefore neglected in further correspondence.*

6.4 Localization of the Anisotropic Error Estimators

For localization, we use the partition of unity (PU) technique presented in [62]. We split our error in a temporal and spatial directional contributions as

$$\begin{aligned} \eta_\tau^p &:= \frac{1}{2} \rho_\tau \left(\mathbf{R}_h^p u_{\tau h}^{p+1} \right) \left(\mathbf{E}_\tau^{(k+1)} \mathbf{R}_h^p z_{\tau h}^{p+1} - \mathbf{R}_h^p z_{\tau h}^{p+1} \right) \\ &\quad + \frac{1}{2} \rho_\tau^* \left(\mathbf{R}_h^p u_{\tau h}^{p+1}, \mathbf{R}_h^p z_{\tau h}^{p+1} \right) \left(\mathbf{E}_\tau^{(k+1)} \mathbf{R}_h^p u_{\tau h}^{p+1} - \mathbf{R}_h^p u_{\tau h}^{p+1} \right), \end{aligned} \quad (54a)$$

$$\eta_{h,i}^p := \frac{1}{2} \rho_\tau \left(\mathbf{R}_h^{p-1,2} u_{\tau h}^{p+1} \right) \left(\mathbf{R}_h^p z_{\tau h}^{p+1} - \mathbf{R}_{h,i}^p z_{\tau h}^{p+1} \right) \quad (54b)$$

$$+ \frac{1}{2} \rho_\tau^* \left(\mathbf{R}_h^{p-1,2} u_{\tau h}^{p+1}, \mathbf{R}_h^{p-1,2} z_{\tau h}^{p+1} \right) \left(\mathbf{R}_h^p u_{\tau h}^{p+1} - \mathbf{R}_{h,i}^p u_{\tau h}^{p+1} \right), \quad (54c)$$

$$\eta_\tau^{p+1} := \frac{1}{2} \rho_\tau \left(u_{\tau h}^{p+1} \right) \left(\mathbf{E}_\tau^{(k+1)} z_{\tau h}^{p+1} - z_{\tau h}^{p+1} \right) + \frac{1}{2} \rho_\tau^* \left(u_{\tau h}^{p+1}, z_{\tau h}^{p+1} \right) \left(\mathbf{E}_\tau^{(k+1)} u_{\tau h}^{p+1} - u_{\tau h}^{p+1} \right), \quad (54d)$$

$$\eta_{h,i}^{p+1} := \frac{1}{2} \rho_\tau \left(\mathbf{R}_h^p u_{\tau h}^{p+1} \right) \left(z_{\tau h}^{p+1} - \mathbf{R}_{h,i}^p z_{\tau h}^{p+1} \right) + \frac{1}{2} \rho_\tau^* \left(\mathbf{R}_h^p u_{\tau h}^{p+1}, \mathbf{R}_h^p z_{\tau h}^{p+1} \right) \left(u_{\tau h}^{p+1} - \mathbf{R}_{h,i}^p u_{\tau h}^{p+1} \right). \quad (54e)$$

To localize the contributions in (54), we use the PU-technique. In particular, we use the functions $\Psi_{\tau,n} := \mathcal{X}_{I_n \times \Omega}$ as the temporal partition of unity and $\Psi_{h,K} := \mathcal{X}_{K \times [0,T]}$ as the spatial one. Here, \mathcal{X}_S denotes the characteristic function of the set S . Of course $\sum_{n=1}^N \Psi_{\tau,n} \equiv 1$ and $\sum_{K \in \mathcal{T}_h} \Psi_{h,K} \equiv 1$. This allows us to recast the estimators in (54) with the localized indicators

$$\eta_\tau^p = \sum_{n=1}^N \eta_{\tau,n}^p, \quad \eta_\tau^{p+1} = \sum_{n=1}^N \eta_{\tau,n}^{p+1}, \quad (55)$$

and

$$\eta_{h,i}^p = \sum_{K \in \mathcal{T}_h} \eta_{h,i}^{p_K}, \quad \eta_{h,i}^{p+1} = \sum_{K \in \mathcal{T}_h} \eta_{h,i}^{p_K+1}. \quad (56)$$

where

$$\begin{aligned} \eta_{\tau,n}^p &:= \frac{1}{2} \rho_\tau (R_h^p u_{\tau h}^{p+1}) ((E_\tau^{(k+1)} R_h^p z_{\tau h}^{p+1} - R_h^p z_{\tau h}^{p+1}) \Psi_{\tau,n}) \\ &\quad + \frac{1}{2} \rho_\tau^* (R_h^p u_{\tau h}^{p+1}, R_h^p z_{\tau h}^{p+1}) ((E_\tau^{(k+1)} R_h^p u_{\tau h}^{p+1} - R_h^p u_{\tau h}^{p+1}) \Psi_{\tau,n}), \end{aligned} \quad (57a)$$

$$\begin{aligned} \eta_{h,i}^{p_K} &:= \frac{1}{2} \rho_\tau (R_h^{p-1,2} u_{\tau h}^{p+1}) ((R_h^p z_{\tau h}^{p+1} - R_{h,i}^p z_{\tau h}^{p+1}) \Psi_{h,K}) \\ &\quad + \frac{1}{2} \rho_\tau^* (R_h^{p-1,2} u_{\tau h}^{p+1}, R_h^{p-1,2} z_{\tau h}^{p+1}) ((R_h^p u_{\tau h}^{p+1} - R_{h,i}^p u_{\tau h}^{p+1}) \Psi_{h,K}), \end{aligned} \quad (57b)$$

$$\begin{aligned} \eta_{\tau,n}^{p+1} &:= \frac{1}{2} \rho_\tau (u_{\tau h}^{p+1}) ((E_\tau^{(k+1)} z_{\tau h}^{p+1} - z_{\tau h}^{p+1}) \Psi_{\tau,n}) \\ &\quad + \frac{1}{2} \rho_\tau^* (u_{\tau h}^{p+1}, z_{\tau h}^{p+1}) ((E_\tau^{(k+1)} u_{\tau h}^{p+1} - u_{\tau h}^{p+1}) \Psi_{\tau,n}), \end{aligned} \quad (57c)$$

$$\begin{aligned} \eta_{h,i}^{p_K+1} &:= \frac{1}{2} \rho_\tau (R_h^p u_{\tau h}^{p+1}) ((z_{\tau h}^{p+1} - R_{h,i}^{p+1} z_{\tau h}^{p+1}) \Psi_{h,K}) \\ &\quad + \frac{1}{2} \rho_\tau^* (R_h^p u_{\tau h}^{p+1}, R_h^p z_{\tau h}^{p+1}) ((u_{\tau h}^{p+1} - R_{h,i}^{p+1} u_{\tau h}^{p+1}) \Psi_{h,K}). \end{aligned} \quad (57d)$$

7 Algorithm for Goal-Oriented Anisotropic hp -Adaptivity

With the goal-oriented error representation and anisotropic indicators in place, we now present the algorithm for goal-oriented anisotropic hp -adaptivity. The elementwise contributions of the anisotropic error indicators in space are given in (56). Following Thm. 6.13, we discard the higher-order spatial remainder of η_h^p and η_h^{p+1} . The temporal slabwise contributions are given in (55). The spatial and temporal indicators drive the anisotropic mesh-adaptation strategy in Alg. 1. By evaluating the directional contributions separately, the marking procedure naturally yields anisotropic refinement when the error is dominated by specific directions, and isotropic refinement when the contributions are balanced.

Remark 7.1 (Anisotropic- hp Adaptation).

- With the spatial mesh fixed across all time slabs, the directional spatial estimators $\eta_{h,i}^{p_K+1}$ and $\eta_{h,i}^{p_K}$ for each $K \in \mathcal{T}_h$ and $i \in \{1, \dots, d\}$ are defined on $K \times [0, T]$, while the time-slab estimators η_τ^p and η_τ^{p+1} on I_n are defined on $\Omega \times I_n$. We use the PU localization from Sec. 6.4, which makes the definition of the localized error estimators straightforward using indicator functions. In the implementation they are calculated as sums of space-time cell contributions. The spatial estimators $\eta_{h,i}^{p_K+1}$ and $\eta_{h,i}^{p_K}$ for a cell $K \in \mathcal{T}_h$ and spatial direction i are obtained by summing over all $I_n \in \mathcal{T}_\tau$, whereas the temporal estimators $\eta_{\tau,n}^{p+1}$ and $\eta_{\tau,n}^p$ on I_n result from summing over all $K \in \mathcal{T}_h$.
- Marking for hp -refinement and coarsening is performed separately in each spatial direction (Alg. 1, l. 12, 13). A cell K is marked for refinement in direction i if $\eta_{h,i}^K$ belongs to the largest $\theta_h|\mathcal{T}_h|$ values among all $d|\mathcal{T}_h|$ directional indicators. We use the local saturation indicators $\gamma_{h,i}^{p_K}$ and a prescribed threshold $\gamma \in (0, 1)$ to decide between h - and p -refinement (Alg. 1, l. 11). We apply local p -enrichment in direction i if $\gamma_{h,i}^{p_K} < \gamma$, indicating significant reduction under enrichment, and local h -refinement otherwise. The same rule is used in time, see (Alg. 1, l. 17 to 20).
- Adaptive h -refinement on quadrilateral or hexahedral meshes leads to interdependent hanging nodes. To resolve these mutual dependencies, we refine the coarser element at the end of the hanging-node chain in the appropriate direction (i. e. anisotropically).

Algorithm 1: Anisotropic mesh adaptation: estimate, mark & refine/coarsen

Require: $\theta_h \in [0, d]$, $\theta_\tau \in [0, 1]$, $\theta_h^{co} \in [0, d - \theta_h]$, $\theta_\tau^{co} \in [0, 1 - \theta_\tau]$, threshold $\gamma > 0$.

1: **SOLVE:**

- 2: Solve **primal** problem (17): Find $u_{\tau h}^p \in \mathcal{X}_{\tau h}^{k,p} : A_{\tau h}(u_{\tau h}^p, w_{\tau h}) = F_{\tau h}(w_{\tau h}) \quad \forall w_{\tau h} \in \mathcal{X}_{\tau h}^{k,p}$.
- 3: Solve **primal ho** problem (17): Find $u_{\tau h}^{p+1} \in \mathcal{X}_{\tau h}^{k,p+1} : A_{\tau h}(u_{\tau h}^{p+1}, w_{\tau h}) = F_{\tau h}(w_{\tau h}) \quad \forall w_{\tau h} \in \mathcal{X}_{\tau h}^{k,p+1}$.
- 4: Solve **adjoint** problem (20): Find $z_{\tau h} \in \mathcal{X}_{\tau h}^{k,p+1} : A_{\tau h}(v_{\tau h}, z_{\tau h}) = J'(u_{\tau h})(v_{\tau h}) \quad \forall v_{\tau h} \in \mathcal{X}_{\tau h}^{k,p+1}$.

5: **ESTIMATE:**

- 6: Compute spatial error indicators $\eta_{h,i}^{p+1}$ and $\eta_{h,i}^{p_K}$ for all $K \in \mathcal{T}_h, i = 1, \dots, d$ (cf. (56)).
- 7: Compute temporal error indicators $\eta_{\tau,n}^{p+1}$ and $\eta_{\tau,n}^p$ for all $I_n \in \mathcal{T}_\tau$ (cf. (55)).

8: **MARK (space):**

- 9: Let $\mathcal{M}_h^{ref} \subset \mathcal{T}_h$ be the set of $\theta_h |\mathcal{T}_h|$ cells K with largest $\eta_{h,i}^{p+1}$, over all directions i .
- 10: Let $\mathcal{M}_h^{co} \subset \mathcal{T}_h$ be the set of $\theta_h^{co} |\mathcal{T}_h|$ cells K with smallest $\eta_{h,i}^{p+1}$, over all directions i .

$$11: \gamma_{h,i}^{p_K} := \eta_{h,i}^{p+1} / \eta_{h,i}^{p_K}$$

- 12: Mark $K \in \mathcal{M}_h^{ref}$ in direction i for anisotropic $\begin{cases} h\text{-refinement} & \text{if } \gamma_{h,i}^{p_K} > \gamma, \\ p\text{-refinement} & \text{otherwise.} \end{cases}$
- 13: Mark $K \in \mathcal{M}_h^{co}$ in direction i for anisotropic $\begin{cases} h\text{-coarsening} & \text{if } \gamma_{h,i}^{p_K} < \gamma, \\ p\text{-coarsening} & \text{otherwise.} \end{cases}$

14: **MARK (time):**

- 15: Let $\mathcal{M}_\tau^{ref} \subset \mathcal{T}_\tau$ be the set of $\theta_\tau |\mathcal{T}_\tau|$ subintervals I_n with largest $\eta_{\tau,n}^p$.
- 16: Let $\mathcal{M}_\tau^{co} \subset \mathcal{T}_\tau$ be the set of $\theta_\tau^{co} |\mathcal{T}_\tau|$ subintervals I_n with smallest $\eta_{\tau,n}^p$.
- 17: $\gamma_\tau^n := \eta_{\tau,n}^{p+1} / \eta_{\tau,n}^p$
- 18: Mark $I_n \in \mathcal{M}_\tau^{ref}$ for τ -refinement if $\gamma_\tau^n > \gamma$ and for k -refinement if $\gamma_\tau^n \leq \gamma$.
- 19: Mark $I_n \in \mathcal{M}_\tau^{co}$ for τ -coarsening if $\gamma_\tau^n < \gamma$ and for k -coarsening if $\gamma_\tau^n \geq \gamma$.

20: **REFINE/COARSEN:** Adapt $(\mathcal{T}_h, \mathcal{T}_\tau)$ according to the spatial and temporal marks.

- *Adaptive p -refinement within discontinuous Galerkin (DG) methods is straightforward, as no continuity is enforced across element interfaces. However, care must be taken to correctly evaluate face integrals. In contrast, conforming methods require constraint equations when using distinct finite elements on two sides of a face to ensure continuity across faces with varying polynomial degrees [14].*

To compute the error indicators required in Alg. 1, we first solve the primal problem forward in time, followed by the adjoint problem backward in time. Using both primal and adjoint solutions, we calculate the local error estimators (56) and (55), perform marking and refinement according to Alg. 1, and repeat the space-time solution procedure iteratively until the desired accuracy is reached. For algorithmic details and implementation aspects of tensor-product space-time finite elements in the deal.II library, we refer to [54, 67, 72, 35]. For implementation aspects of hp methods in deal.II we refer to [39, 14].

8 Solver for the Algebraic Systems

We use the decoupling of the system at interval endpoints and solve the space-time system in Prob. 4.3 via a time-marching approach. For the local problems on I_n we use GMRES with a preconditioner that further decouples the temporal degrees of freedom by an LU-then-diagonalize construction of the temporal operator. This follows the ideas of Axelsson and Neytcheva [8] and can later enable parallelism in time [57]. The general idea of decoupling large block systems in space-time discretizations has been explored earlier [74, 65]. In general, for $k \in \{0\} \cup \mathbb{N}$, let

$$G^k := (M_\tau^k)^{-1} A_\tau^k \in \mathbb{R}^{(k+1) \times (k+1)}, \quad G^k = L^k U^k, \quad \text{diag}(U^k) = \mathbb{1}_{k+1}, \quad (58)$$

Space-time system on I_n with $|I_n| = \tau_n$ and order k_n

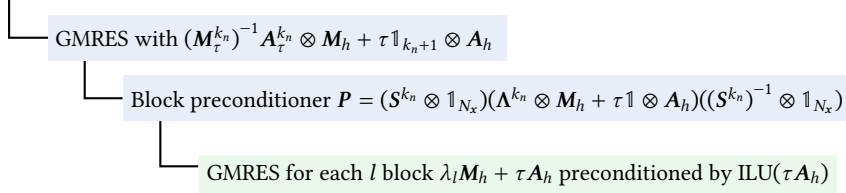


Figure 2: Sketch of the linear solution process: The space-time system on I_n is preconditioned by a GMRES method to which we apply a block preconditioner based on the diagonalization of $\text{tril}((M_\tau^{k_n})^{-1} A_\tau)$. The diagonal blocks are then solved with few iterations of a preconditioned GMRES method.

be an LU factorization with unit diagonal in the upper factor. For a given slab I_n , we multiply Prob. 4.2 by $(M_\tau^{k_n})^{-1}$. Then, the system matrix in Prob. 4.2 can be written as

$$G^{k_n} \otimes M_h + \tau 1_k \otimes A_h. \quad (59)$$

We compute an eigen-decomposition of L^{k_n} , the lower factor of G^{k_n} , $L^{k_n} = S^{k_n} \Lambda^{k_n} (S^{k_n})^{-1}$, $\Lambda = \text{diag}(\lambda_1, \dots, \lambda_{k_n+1})$. This yields the block-diagonal preconditioner to the system (59)

$$P := (S^{k_n} \otimes 1_{N_x})(\Lambda \otimes M_h + 1_k \otimes \tau A_h)((S^{k_n})^{-1} \otimes 1_{N_x}), \quad (60)$$

so that applying P^{-1} decouples the time dimension into k independent spatial solves,

$$(\lambda_\ell M_h + \tau A_h) z_\ell = r_\ell, \quad \ell = 1, \dots, k_n + 1, \quad (61)$$

each of which can be equipped with a suitable spatial preconditioner (e.g. an ILU for τA_h). In our implementation, this preconditioning and solver technique is applied to Prob. (4.5) in an analogous manner.

9 Numerical Examples

To validate the efficacy of our anisotropic hp -refinement strategy for time-dependent CDR equations, we present three benchmark problems:

1. *Interior Layer Problem*: An exact solution is available and features a sharp interior layer, serving as a reference for accuracy and convergence studies.
2. *Instationary Hemker Problem*: This classical benchmark models convection-dominated heat transfer around a hot cylindrical obstacle, leading to both boundary and interior layers.
3. *Fichera corner*: In the typical domain with edge and corner singularities, an initial concentration is transported towards these singularities.

In all cases, we apply anisotropic hp -refinement in space and time, allowing for independent adjustment of the mesh size and polynomial degree in each coordinate direction. No restrictions are imposed on the variation of polynomial degrees within or across elements. To assess the accuracy of the goal-oriented error estimator, we study the *effectivity index*

$$I_{\text{eff}} = \left| \frac{\eta_h^{a, p+1} + \eta_\tau^{p+1}}{J(u) - J(u_{\tau h})} \right|, \quad (62)$$

where $\eta_h^{a,p+1} := \sum_{i=1}^d \eta_{h,i}^{p+1}$. The sum of the spatial and temporal error estimators is denoted by $\eta_{th}^{a,p+1} = \eta_h^{a,p+1} + \eta_\tau^{p+1}$. For the sake of brevity, we subsequently drop the $p+1$ superscript. As an indicator of mesh anisotropy, we track the maximum aspect ratio, defined by

$$\rho_{\max} := \max_{K \in \mathcal{T}_h} \rho_K, \quad (63)$$

where ρ_K is given by (8). We denote the total number of DoFs by N_{tot} , and split them into spatial and temporal DoFs N_x and N_t , respectively. All simulations are implemented using the deal.II finite element library [1] and executed on one node of the HSUPER HPC cluster at Helmut Schmidt University, equipped with two Intel Xeon Platinum 8360Y CPUs and 1024 GB of RAM.

9.1 Interior Layer

This well-known benchmark has an exact solution

$$u(\mathbf{x}, t) = \frac{e^{3(t-1.0)}}{2} \left(1 - \tanh \frac{2x - y - \frac{1}{2}}{\sqrt{5}\varepsilon} \right) \quad (64)$$

with a sharp interior layer, of thickness $\mathcal{O}(\sqrt{\varepsilon} |\log \varepsilon|)$. The problem is defined on $\Omega \times I = (0, 1)^2 \times (0, 1]$ with inhomogeneous boundary conditions given by (64) on the whole boundary $\Gamma_D = \partial\Omega$. The convection is set to $\mathbf{b} = \frac{1}{\sqrt{5}}(1, 2)^\top$, the diffusion to $\varepsilon = 10^{-6}$ or $\varepsilon = 10^{-8}$ and the reaction coefficient is given by $\alpha = 1$. As sketched in Fig. 3, we employ unstructured meshes to solve the problem. We consider two different goal functionals: the L^2 error in space-time

$$J(u) = \frac{1}{\|e\|_{\Omega \times I}} \int_I (u, e) dt, \quad \text{with } \|\cdot\|_{\Omega \times I} = \left(\int_I (\cdot, \cdot) dt \right)^{\frac{1}{2}}, \quad e := u - u_{th}. \quad (65)$$

and a point value control inside the interior layer at final time

$$J(u) = u(\mathbf{x}_c, T), \quad \text{where } \mathbf{x}_c = \left(\frac{1}{2}, \frac{1}{2} \right). \quad (66)$$

We regularize the point functional (66) by a regularized Dirac delta function $\delta_{s,\mathbf{x}_c}(r) = \alpha e^{(1-1/(1-r^2/s^2))}$, where $r = \|\mathbf{x} - \mathbf{x}_c\|$, $s > 0$ is the cutoff radius and α the scaling factor, such that δ_{s,\mathbf{x}_c} integrates to 1. In all configurations, we refine and coarsen a fixed fraction of cells in both space and time. In space and time, the refinement fraction is set to $\theta_{\text{space}}^{\text{ref}} = \theta_{\text{time}}^{\text{ref}} = \frac{1}{8}$, and the coarsening fraction is $\theta_{\text{space}}^{\text{co}} = \theta_{\text{time}}^{\text{co}} = \frac{1}{25}$. We use polynomial degrees $1 \leq p, k \leq 9$ in space and time, without imposing restrictions on their variation within a cell or across neighboring cells. The initial space-time triangulation consists of a single time cell and a once uniformly refined spatial coarse mesh (cf. Fig. 3).

Space-time L^2 error control. Tab. 1 demonstrates good control of the L^2 error with effectivity indices I_{eff} remaining close to 1 over a wide range of refinements, indicating accurate and reliable a posteriori error estimation even with anisotropic hp refinements. Moreover, the maximum aspect ratio ρ_{\max} increases significantly, reaching values above 6000, which underscores the robustness of the method with respect to highly anisotropic elements. This confirms the capability of the refinement strategy to efficiently resolve anisotropic features, such as the interior layer, while maintaining effectivity. Fig 3 shows a plot of the solution with the highly refined mesh along the interior layer.

Point value control. To demonstrate that our anisotropic hp -refinement strategy generalizes well across a range of convection-dominated regimes, we test two diffusion coefficients $\varepsilon = 10^{-6}$ and $\varepsilon = 10^{-8}$.

In Fig. 4, we show the anisotropic hp -mesh obtained in the final DWR loop for $\varepsilon = 10^{-6}$. Strong local anisotropy in both mesh size and polynomial degree is observed close to the goal point. Highly refined

Table 1: Number of DoFs, error estimators, error, and effectivity index for the step-layer benchmark with L^2 space-time error control (65) and diffusion coefficient $\varepsilon = 10^{-6}$.

ℓ	$ \mathcal{T}_h $	N_x^{lo}	N_x^{ho}	N_t	work	ρ_{\max}	$\eta_{h,1}$	$\eta_{h,2}$	η_h^a	η_τ	$\eta_{\tau h}^a$	e	I_{eff}
0	40	160	360	2	$3.52 \cdot 10^3$	4.20	$-8.59 \cdot 10^{-3}$	$-4.96 \cdot 10^{-3}$	$-1.36 \cdot 10^{-2}$	$-1.59 \cdot 10^{-2}$	$-2.95 \cdot 10^{-2}$	$1.72 \cdot 10^{-1}$	0.17
1	40	182	392	3	$7.64 \cdot 10^3$	4.20	$-3.39 \cdot 10^{-2}$	$-1.18 \cdot 10^{-2}$	$-4.57 \cdot 10^{-2}$	$-3.20 \cdot 10^{-3}$	$-4.89 \cdot 10^{-2}$	$4.14 \cdot 10^{-2}$	1.18
2	40	203	423	3	$8.53 \cdot 10^3$	4.20	$-3.04 \cdot 10^{-2}$	$-9.99 \cdot 10^{-3}$	$-4.04 \cdot 10^{-2}$	$-2.91 \cdot 10^{-3}$	$-4.33 \cdot 10^{-2}$	$4.14 \cdot 10^{-2}$	1.05
3	40	223	453	3	$1.00 \cdot 10^4$	4.20	$-2.87 \cdot 10^{-2}$	$-9.47 \cdot 10^{-3}$	$-3.82 \cdot 10^{-2}$	$-2.91 \cdot 10^{-3}$	$-4.11 \cdot 10^{-2}$	$4.14 \cdot 10^{-2}$	0.99
4	40	243	483	3	$1.09 \cdot 10^4$	4.20	$-2.76 \cdot 10^{-2}$	$-9.11 \cdot 10^{-3}$	$-3.67 \cdot 10^{-2}$	$-2.91 \cdot 10^{-3}$	$-3.96 \cdot 10^{-2}$	$4.14 \cdot 10^{-2}$	0.96
5	40	263	513	3	$1.18 \cdot 10^4$	4.20	$-2.68 \cdot 10^{-2}$	$-8.88 \cdot 10^{-3}$	$-3.57 \cdot 10^{-2}$	$-2.91 \cdot 10^{-3}$	$-3.86 \cdot 10^{-2}$	$4.14 \cdot 10^{-2}$	0.93
6	40	283	543	3	$1.27 \cdot 10^4$	4.20	$-2.63 \cdot 10^{-2}$	$-8.71 \cdot 10^{-3}$	$-3.50 \cdot 10^{-2}$	$-2.91 \cdot 10^{-3}$	$-3.79 \cdot 10^{-2}$	$4.14 \cdot 10^{-2}$	0.92
7	40	303	573	3	$1.27 \cdot 10^4$	4.20	$-2.59 \cdot 10^{-2}$	$-8.58 \cdot 10^{-3}$	$-3.45 \cdot 10^{-2}$	$-2.91 \cdot 10^{-3}$	$-3.74 \cdot 10^{-2}$	$4.14 \cdot 10^{-2}$	0.90
8	40	323	603	3	$1.36 \cdot 10^4$	4.20	$-2.56 \cdot 10^{-2}$	$-8.47 \cdot 10^{-3}$	$-3.41 \cdot 10^{-2}$	$-2.91 \cdot 10^{-3}$	$-3.70 \cdot 10^{-2}$	$4.14 \cdot 10^{-2}$	0.89
11	70	898	1545	4	$6.47 \cdot 10^4$	$2.99 \cdot 10^1$	$-1.29 \cdot 10^{-2}$	$-4.13 \cdot 10^{-3}$	$-1.70 \cdot 10^{-2}$	$6.81 \cdot 10^{-4}$	$-1.63 \cdot 10^{-2}$	$1.08 \cdot 10^{-2}$	1.51
12	87	1215	2060	4	$8.75 \cdot 10^4$	$5.98 \cdot 10^1$	$-7.21 \cdot 10^{-3}$	$-2.48 \cdot 10^{-3}$	$-9.69 \cdot 10^{-3}$	$7.87 \cdot 10^{-4}$	$-8.90 \cdot 10^{-3}$	$7.84 \cdot 10^{-3}$	1.14
23	884	22 962	34 441	7	$4.02 \cdot 10^6$	$6.12 \cdot 10^3$	$1.39 \cdot 10^{-5}$	$-1.41 \cdot 10^{-6}$	$1.25 \cdot 10^{-5}$	$-1.79 \cdot 10^{-8}$	$1.25 \cdot 10^{-5}$	$2.44 \cdot 10^{-5}$	0.51

Table 2: Number of DoFs, error estimators, error, and effectivity indices for the step-layer benchmark with point value control (66) and diffusion coefficient $\varepsilon = 10^{-6}$.

ℓ	$ \mathcal{T}_h $	N_x^{lo}	N_x^{ho}	N_t	work	ρ_{\max}	$\eta_{h,1}$	$\eta_{h,2}$	η_h^a	η_τ	$\eta_{\tau h}^a$	e	I_{eff}
0	40	160	360	2	$2.88 \cdot 10^3$	4.20	9.68	2.61	$1.23 \cdot 10^{-1}$	$3.44 \cdot 10^{-1}$	$1.26 \cdot 10^{-1}$	$1.10 \cdot 10^{-1}$	114.82
1	40	185	396	2	$3.33 \cdot 10^3$	4.20	$1.32 \cdot 10^{-1}$	$2.11 \cdot 10^{-1}$	$1.34 \cdot 10^{-1}$	1.20	$1.46 \cdot 10^{-1}$	$1.15 \cdot 10^{-1}$	127.05
2	42	231	467	2	$4.16 \cdot 10^3$	4.20	$2.54 \cdot 10^{-1}$	$3.10 \cdot 10^{-1}$	$2.57 \cdot 10^{-1}$	2.45	$2.82 \cdot 10^{-1}$	$1.18 \cdot 10^{-1}$	238.64
3	44	273	532	2	$5.46 \cdot 10^3$	4.20	$2.37 \cdot 10^{-1}$	$4.32 \cdot 10^{-1}$	$2.41 \cdot 10^{-1}$	4.02	$2.82 \cdot 10^{-1}$	$1.18 \cdot 10^{-1}$	238.56
4	49	362	669	2	$7.24 \cdot 10^3$	6.10	3.29	$-7.19 \cdot 10^{-2}$	3.22	1.76	4.98	$1.18 \cdot 10^{-1}$	42.18
5	56	474	842	3	$1.85 \cdot 10^4$	$1.15 \cdot 10^1$	$4.33 \cdot 10^{-1}$	$1.06 \cdot 10^{-1}$	$5.39 \cdot 10^{-1}$	$6.56 \cdot 10^{-2}$	$6.05 \cdot 10^{-1}$	$1.41 \cdot 10^{-1}$	4.29
6	56	539	922	3	$2.10 \cdot 10^4$	$1.15 \cdot 10^1$	$3.07 \cdot 10^{-1}$	$1.08 \cdot 10^{-2}$	$3.18 \cdot 10^{-1}$	$-4.21 \cdot 10^{-2}$	$2.76 \cdot 10^{-1}$	$2.06 \cdot 10^{-1}$	1.34
7	56	611	1009	3	$2.38 \cdot 10^4$	$1.15 \cdot 10^1$	$3.57 \cdot 10^{-1}$	$2.47 \cdot 10^{-2}$	$3.82 \cdot 10^{-1}$	$-2.84 \cdot 10^{-2}$	$3.53 \cdot 10^{-1}$	$2.91 \cdot 10^{-1}$	1.21
14	181	10 373	13 100	6	$1.21 \cdot 10^6$	$2.39 \cdot 10^2$	$-2.79 \cdot 10^{-7}$	$-1.14 \cdot 10^{-7}$	$-3.93 \cdot 10^{-7}$	$4.79 \cdot 10^{-5}$	$4.75 \cdot 10^{-5}$	$-2.95 \cdot 10^{-5}$	1.61
15	249	16 862	20 974	7	$2.54 \cdot 10^6$	$4.68 \cdot 10^2$	$9.00 \cdot 10^{-8}$	$-1.96 \cdot 10^{-7}$	$-1.06 \cdot 10^{-7}$	$-2.55 \cdot 10^{-6}$	$-2.66 \cdot 10^{-6}$	$5.56 \cdot 10^{-7}$	4.78
16	250	16 980	21 115	9	$4.28 \cdot 10^6$	$3.83 \cdot 10^2$	$6.71 \cdot 10^{-8}$	$-1.46 \cdot 10^{-7}$	$-7.89 \cdot 10^{-8}$	$-1.87 \cdot 10^{-8}$	$-9.76 \cdot 10^{-8}$	$4.20 \cdot 10^{-7}$	0.23
17	350	26 953	33 184	9	$6.55 \cdot 10^6$	$3.83 \cdot 10^2$	$3.38 \cdot 10^{-8}$	$-3.89 \cdot 10^{-8}$	$-5.17 \cdot 10^{-9}$	$-1.38 \cdot 10^{-8}$	$-1.90 \cdot 10^{-8}$	$-2.89 \cdot 10^{-9}$	6.58
18	490	40 943	50 113	9	$9.95 \cdot 10^6$	$3.83 \cdot 10^2$	$4.89 \cdot 10^{-8}$	$-2.40 \cdot 10^{-8}$	$-2.49 \cdot 10^{-8}$	$-2.26 \cdot 10^{-8}$	$2.30 \cdot 10^{-9}$	$-1.66 \cdot 10^{-9}$	1.39

Table 3: Number of DoFs, error estimators, error, and effectivity indices for the step-layer benchmark with point value control (66) and diffusion coefficient $\varepsilon = 10^{-8}$.

ℓ	$ \mathcal{T}_h $	N_x^{lo}	N_x^{ho}	N_t	work	ρ_{\max}	$\eta_{h,1}$	$\eta_{h,2}$	η_h^a	η_τ	$\eta_{\tau h}^a$	e	I_{eff}
0	40	160	360	2	$2.88 \cdot 10^3$	4.20	9.69	2.61	$1.23 \cdot 10^{-1}$	$3.43 \cdot 10^{-1}$	$1.26 \cdot 10^{-1}$	$-7.63 \cdot 10^{-2}$	165.00
1	40	183	393	2	$3.29 \cdot 10^3$	4.20	$1.32 \cdot 10^{-1}$	$2.02 \cdot 10^{-1}$	$1.34 \cdot 10^{-1}$	1.15	$1.46 \cdot 10^{-1}$	$-7.16 \cdot 10^{-2}$	204.00
2	42	223	456	2	$4.01 \cdot 10^3$	4.20	$2.81 \cdot 10^{-1}$	$6.59 \cdot 10^{-1}$	$2.88 \cdot 10^{-1}$	2.65	$3.15 \cdot 10^{-1}$	$-6.84 \cdot 10^{-2}$	461.00
3	46	274	542	2	$5.48 \cdot 10^3$	4.20	$2.58 \cdot 10^{-1}$	$4.04 \cdot 10^{-1}$	$2.62 \cdot 10^{-1}$	2.78	$2.90 \cdot 10^{-1}$	$-6.84 \cdot 10^{-2}$	424.00
4	52	339	654	2	$6.78 \cdot 10^3$	6.10	$1.64 \cdot 10^{-1}$	$1.53 \cdot 10^{-1}$	$1.66 \cdot 10^{-1}$	1.81	$1.84 \cdot 10^{-1}$	$-6.84 \cdot 10^{-2}$	269.00
5	60	429	804	2	$8.58 \cdot 10^3$	$1.15 \cdot 10^1$	1.92	$1.68 \cdot 10^{-2}$	1.94	$8.42 \cdot 10^{-1}$	2.78	$-9.28 \cdot 10^{-2}$	30.00
6	60	489	879	3	$1.91 \cdot 10^4$	$1.15 \cdot 10^1$	$3.10 \cdot 10^{-1}$	$-7.29 \cdot 10^{-3}$	$3.03 \cdot 10^{-1}$	$6.66 \cdot 10^{-2}$	$3.69 \cdot 10^{-1}$	$2.08 \cdot 10^{-2}$	17.80
7	60	557	962	3	$2.17 \cdot 10^4$	$1.15 \cdot 10^1$	$1.86 \cdot 10^{-1}$	$-1.26 \cdot 10^{-2}$	$1.73 \cdot 10^{-1}$	$1.03 \cdot 10^{-2}$	$1.83 \cdot 10^{-1}$	$-7.65 \cdot 10^{-2}$	2.39
8	60	634	1054	3	$2.47 \cdot 10^4$	$1.15 \cdot 10^1$	$7.47 \cdot 10^{-2}$	$1.21 \cdot 10^{-2}$	$8.68 \cdot 10^{-2}$	$1.86 \cdot 10^{-2}$	$1.05 \cdot 10^{-1}$	$-1.37 \cdot 10^{-2}$	7.67
21	1245	112 689	137 154	7	$1.74 \cdot 10^7$	$1.79 \cdot 10^3$	$4.09 \cdot 10^{-9}$	$-3.89 \cdot 10^{-7}$	$-3.85 \cdot 10^{-7}$	$-2.67 \cdot 10^{-6}$	$-3.06 \cdot 10^{-6}$	$5.05 \cdot 10^{-6}$	0.61
22	1633	150 792	183 289	8	$2.90 \cdot 10^7$	$1.90 \cdot 10^3$	$6.15 \cdot 10^{-10}$	$-1.23 \cdot 10^{-6}$	$-1.23 \cdot 10^{-6}$	$2.51 \cdot 10^{-7}$	$-9.80 \cdot 10^{-7}$	$3.21 \cdot 10^{-7}$	3.05
23	2153	201 159	244 348	8	$3.86 \cdot 10^7$	$1.90 \cdot 10^3$	$7.63 \cdot 10^{-10}$	$-4.44 \cdot 10^{-8}$	$-4.36 \cdot 10^{-8}$	$2.52 \cdot 10^{-8}$	$-1.84 \cdot 10^{-8}$	$1.63 \cdot 10^{-8}$	1.13

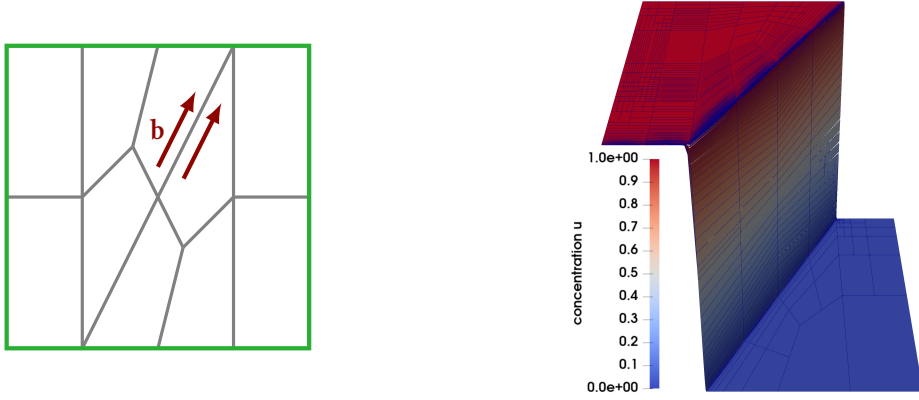


Figure 3: Geometry and coarse, unstructured mesh of the domain (left) and the best adaptive solution obtained for the L^2 space-time error control. On the left, green coloring corresponds to inhomogeneous Dirichlet BCs.

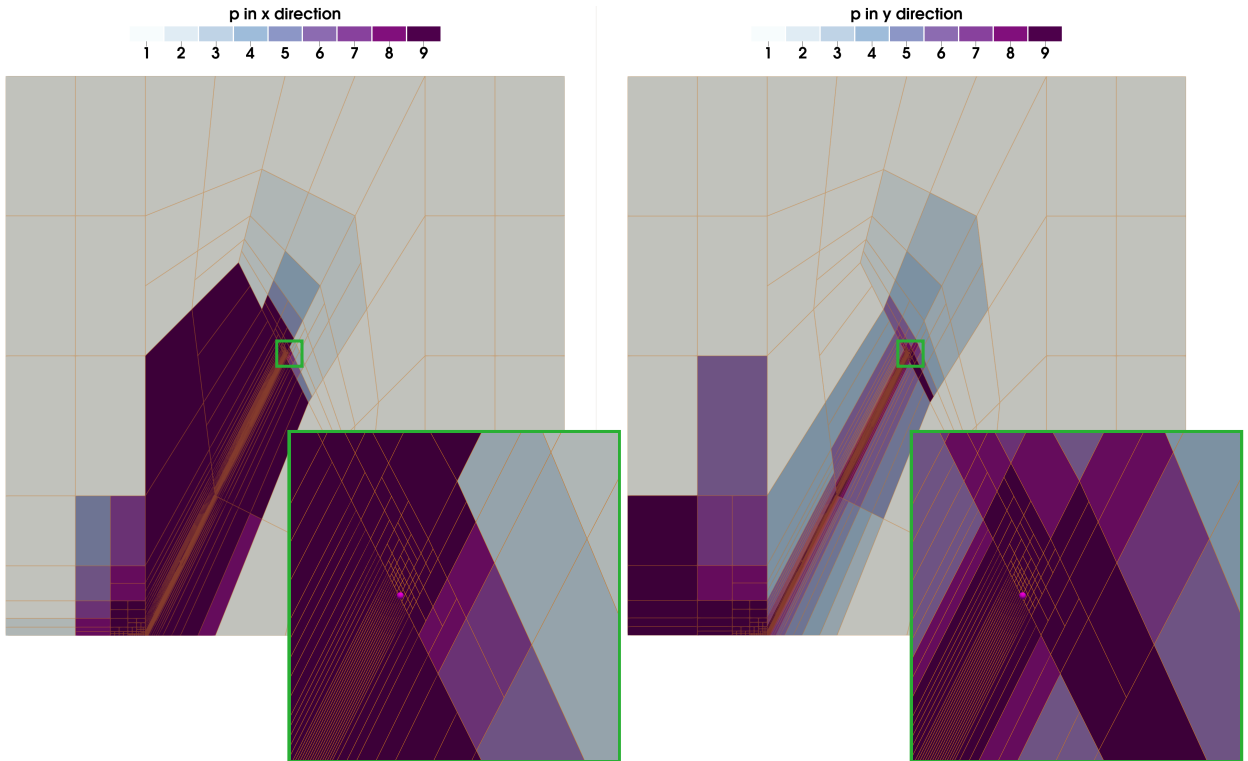


Figure 4: Anisotropic hp -mesh after 18 refinement steps (cf. Tables 2) with diffusion coefficient $\varepsilon = 10^{-6}$. The green squares are zoomed in to visualize the high anisotropic h and p refinement around the goal point. Within the mesh we observe high anisotropies in the mesh size and polynomial degree.

elements are aligned with the interior layer. Far from x_c , we observe no refinement in h and p . Note that we observe cells with linear polynomials in one and 9th order polynomials in the other direction.

Tables 2 and 3 show that the pointwise error converges very fast under anisotropic hp -refinement. While the initial effectivity indices I_{eff} are high due to overestimation in the early refinement stages, they stabilize toward moderate values as the mesh better resolves the behavior close to the evaluation point. The maximum aspect ratio ρ_{\max} increases substantially, highlighting the method's robustness in resolving localized features with strongly anisotropic elements. These results confirm that the employed refinement strategy is highly effective for accurate pointwise error control. Fig. 5 underscores that the

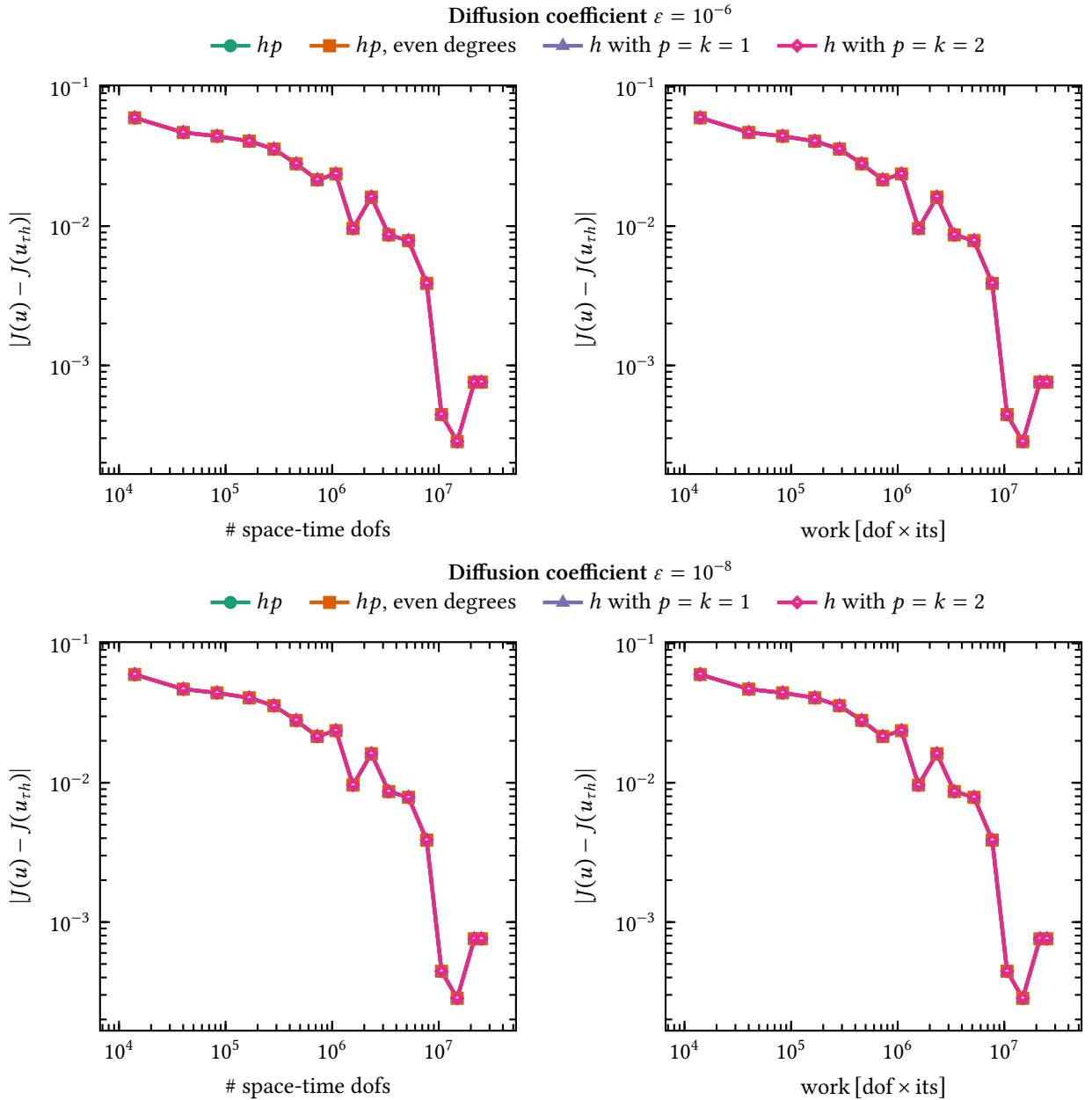


Figure 5: Comparison between adaptive anisotropic refinement strategies: anisotropic hp refinement considering all polynomials $p, k \in \{1, \dots, 9\}$ and only even polynomials $p, k \in \{2, 4, 6, 8, 10\}$. To validate the efficiency of the anisotropic hp refinement we consider h anisotropic refinement with isotropic linear and quadratic polynomial degree (uniform in space and time).

anisotropic hp -refinement strategy, employing either the full range $p, k \in \{1, \dots, 9\}$ or only even degrees $p, k \in \{2, 4, 6, 8, 10\}$, achieves exponential convergence of the error $|J(u) - J(u_{th})|$ with respect to the number of degrees of freedom. Thus, this strategy clearly outperforms anisotropic h -refinement with fixed polynomial degree ($p = k = 1$ or $p = k = 2$). Although a pre-asymptotic regime is visible in the convergence behavior, the results clearly demonstrate the superior approximation efficiency of the anisotropic hp -refinement strategy. Notably, the smaller the diffusion coefficient ($\varepsilon = 10^{-6}$ and $\varepsilon = 10^{-8}$), the more pronounced the performance gains of anisotropic hp -refinement, which efficiently resolves the increasingly localized features of the solution. We also observe exponential convergence of the error $|J(u) - J(u_{th})|$ with respect to the computational work w , defined by

$$w = \sum_{i=1}^{|T_r|} (k_i + 1) \cdot N^x \cdot N_i^{it}, \quad (67)$$

where N_i^{it} is the number of GMRES iterations required to solve the local subproblem on the time interval I_i . This metric accounts for the full computational cost of solving the global space-time problem. Notably, the same exponential convergence behavior observed with respect to the number of degrees of freedom is retained when measured against the work. This highlights the efficiency and scalability of the overall approach and confirms the robustness of the linear solver introduced in Sec. 8. The restriction to even polynomial degrees can lead to a more economical discretization by accelerating error reduction in the goal functional and allowing the method to leave the pre-asymptotic regime earlier.

Overall, we observe exponential convergence of the point value error with respect to both degrees of freedom and work. Despite extreme anisotropies (aspect ratios > 1900) and high polynomial degrees, the solver remains robust and efficient. While the spatial and temporal estimator contributions initially differ by orders of magnitude, refinement balances them. This shows the effectiveness of goal-oriented refinement in concentrating resolution where needed for accurate point value control.

9.2 Instationary Hemker Example

We investigate the classical Hemker problem [48] in a time-dependent setting. We consider the convection-diffusion-reaction system given by equation (2), and we set $\alpha = 0$ and $f = 0$, $\mathbf{b} = (1, 0)^\top$. The diffusion coefficient is $\varepsilon = 10^{-4}$ or $\varepsilon = 10^{-6}$. This guarantees that the heat is entirely advected through the domain without any inherent degradation. Consequently, any observed decrease in heat arises solely from numerical artifacts, aside from a negligible reduction induced by the diffusion term. The computational space-time domain is defined as $\Omega \times I$ with $I = (0, 10]$ and $\Omega = ((-3, 8) \times (-3, 3)) \setminus \{(x, y) : x^2 + y^2 \leq 1\}$, illustrated with the coarse mesh in Fig. 6. The boundary conditions are specified as follows: The boundaries colored green in Fig. 6 correspond to Dirichlet boundary conditions. Specifically, the boundary at $x = -3$ is subjected to homogeneous Dirichlet conditions $u = 0$. The boundaries colored blue indicate homogeneous Neumann boundary conditions $\partial_n u = 0$. On the circular boundary, inhomogeneous Dirichlet boundary conditions are imposed with $u = 1$. The aim is to control the error within a control point in the upper interior layer $\mathbf{x}_c = (4, 1)$. To this end, we use the goal functional

$$J(u) = u(\mathbf{x}_c, T). \quad (68)$$

We regularize J by a regularized Dirac delta function $\delta_{s, \mathbf{x}_c}(r)$. We refine and coarsen a fixed fraction of cells in both space and time. In space and time, the refinement fraction is set to $\theta_{\text{space}}^{\text{ref}} = \frac{1}{7}$ and $\theta_{\text{time}}^{\text{ref}} = \frac{1}{8}$. The coarsening fraction is set to $\theta_{\text{space}}^{\text{co}} = \theta_{\text{time}}^{\text{co}} = \frac{1}{25}$. We use polynomial degrees $1 \leq p \leq 9$ and $0 \leq k \leq 9$ in space and time, respectively. We do not put any restrictions on their variation within a cell or across neighboring cells. The initial space-time triangulation consists of the three times uniformly refined time domain I and a twice uniformly refined spatial coarse mesh (cf. Fig. 6).

Tables 4 and 5 summarize the adaptive refinement process for the Hemker problem with $\varepsilon = 10^{-4}$ and $\varepsilon = 10^{-6}$, respectively. For the less convection-dominated case $\varepsilon = 10^{-4}$ the final combined error η_{th}^a is

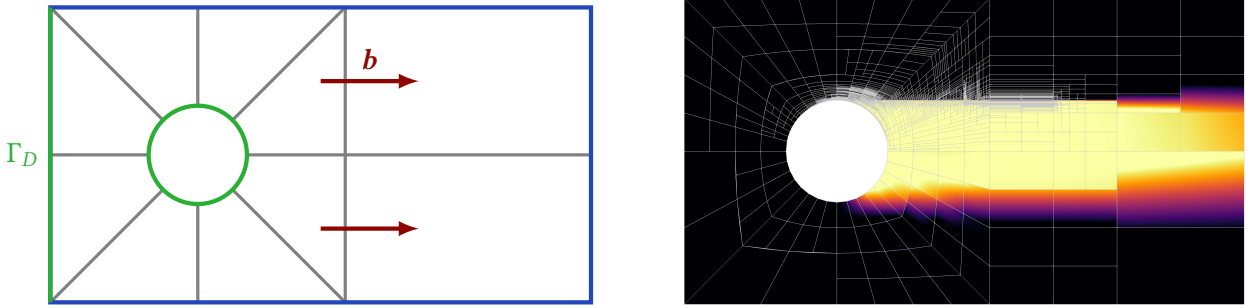


Figure 6: On the left: Geometry and coarse mesh of the domain for the Hemker problem. Green coloring corresponds to Dirichlet BCs, blue indicates homogeneous Neumann BCs. On the circle, inhomogeneous Dirichlet BCs are prescribed. The left boundary is associated with homogeneous Dirichlet BCs. On the right: The solution with mesh at the final time point after the 20th DWR loop with $\varepsilon = 10^{-6}$.

Table 4: Number of DoFs, error estimators, error, and effectivity index for the Hemker benchmark with point value control (68) and diffusion coefficient $\varepsilon = 10^{-4}$.

ℓ	$ \mathcal{T}_h $	N_x^{lo}	N_x^{ho}	N_t	work	ρ_{\max}	$\eta_{h,1}$	$\eta_{h,2}$	η_h^a	η_τ	$\eta_{\tau h}^a$
0	160	640	1440	8	$1.02 \cdot 10^4$	4.10	$-6.58 \cdot 10^{-4}$	$2.44 \cdot 10^{-4}$	$-4.14 \cdot 10^{-4}$	$7.06 \cdot 10^{-5}$	$-3.43 \cdot 10^{-4}$
1	165	763	1632	8	$1.22 \cdot 10^4$	4.60	$-5.41 \cdot 10^{-3}$	$-5.34 \cdot 10^{-3}$	$-1.08 \cdot 10^{-2}$	$-2.03 \cdot 10^{-2}$	$-3.10 \cdot 10^{-2}$
2	173	912	1861	8	$1.46 \cdot 10^4$	4.60	$-8.21 \cdot 10^{-4}$	$-1.71 \cdot 10^{-3}$	$-2.53 \cdot 10^{-3}$	$-1.67 \cdot 10^{-2}$	$-1.92 \cdot 10^{-2}$
3	177	1077	2094	8	$1.72 \cdot 10^4$	6.70	$-2.75 \cdot 10^{-4}$	$-6.21 \cdot 10^{-3}$	$-6.48 \cdot 10^{-3}$	$-1.82 \cdot 10^{-2}$	$-2.46 \cdot 10^{-2}$
4	185	1275	2386	8	$2.04 \cdot 10^4$	6.70	$2.18 \cdot 10^{-3}$	$2.55 \cdot 10^{-4}$	$2.44 \cdot 10^{-3}$	$-2.20 \cdot 10^{-2}$	$-1.95 \cdot 10^{-2}$
5	193	1478	2687	9	$4.43 \cdot 10^4$	6.70	$2.11 \cdot 10^{-3}$	$2.76 \cdot 10^{-3}$	$4.87 \cdot 10^{-3}$	$-1.74 \cdot 10^{-2}$	$-1.25 \cdot 10^{-2}$
6	197	1670	2956	9	$5.01 \cdot 10^4$	6.70	$2.58 \cdot 10^{-3}$	$7.98 \cdot 10^{-4}$	$3.38 \cdot 10^{-3}$	$-1.71 \cdot 10^{-2}$	$-1.38 \cdot 10^{-2}$
7	211	2071	3534	9	$6.21 \cdot 10^4$	6.90	$2.38 \cdot 10^{-3}$	$-2.12 \cdot 10^{-4}$	$2.17 \cdot 10^{-3}$	$-1.62 \cdot 10^{-2}$	$-1.40 \cdot 10^{-2}$
8	226	2484	4139	9	$7.45 \cdot 10^4$	$1.33 \cdot 10^1$	$1.71 \cdot 10^{-3}$	$-2.84 \cdot 10^{-3}$	$-1.12 \cdot 10^{-3}$	$-1.55 \cdot 10^{-2}$	$-1.66 \cdot 10^{-2}$
9	255	3568	5647	9	$1.07 \cdot 10^5$	$1.33 \cdot 10^1$	$-2.53 \cdot 10^{-5}$	$3.73 \cdot 10^{-4}$	$3.47 \cdot 10^{-4}$	$-1.60 \cdot 10^{-2}$	$-1.56 \cdot 10^{-2}$
10	319	6251	9304	10	$3.31 \cdot 10^5$	$1.33 \cdot 10^1$	$1.83 \cdot 10^{-5}$	$-7.29 \cdot 10^{-5}$	$-5.46 \cdot 10^{-5}$	$-1.48 \cdot 10^{-2}$	$-1.48 \cdot 10^{-2}$
14	742	30 148	40 206	12	$2.95 \cdot 10^6$	$1.07 \cdot 10^2$	$2.11 \cdot 10^{-8}$	$-3.93 \cdot 10^{-3}$	$-3.93 \cdot 10^{-3}$	$-9.30 \cdot 10^{-4}$	$-4.86 \cdot 10^{-3}$
15	908	42 201	55 302	12	$4.14 \cdot 10^6$	$1.07 \cdot 10^2$	$8.68 \cdot 10^{-7}$	$-1.37 \cdot 10^{-3}$	$-1.36 \cdot 10^{-3}$	$-2.67 \cdot 10^{-3}$	$-4.04 \cdot 10^{-3}$
16	1163	62 682	80 664	12	$6.46 \cdot 10^6$	$1.07 \cdot 10^2$	$-2.26 \cdot 10^{-7}$	$-5.75 \cdot 10^{-5}$	$-5.77 \cdot 10^{-5}$	$-6.48 \cdot 10^{-4}$	$-7.06 \cdot 10^{-4}$

smaller for comparable computational effort. The more convection-dominated case $\varepsilon = 10^{-6}$ requires a significantly larger number of cells and degrees of freedom to achieve comparable error reduction. This is due to the need to resolve significantly thinner boundary and interior layers. Moreover, the indicators start higher and decay more slowly, underscoring the difficulty of the Hemker problem in this regime. The maximal anisotropy increases throughout the refinement process, reaching values up to 427 and 107, indicating a strong preference for anisotropic refinement in space. The space-time error estimate $\eta_{\tau h}^a$ consistently decreases, demonstrating the effectiveness of the goal-oriented adaptive strategy. These results highlight the potential of the anisotropic hp -adaptive algorithm to effectively address practically relevant, convection-dominated problems.

The left part of Fig. 7 shows refinement concentrated around the obstacle and upstream of the goal point x_c . The zoomed panels highlight the isoparametric curved cells close to the obstacle and the solution close to the goal point. The cut-line plots in Fig. 8 indicate that the solution remains free of spurious oscillations despite the convection-dominated setting. The steep gradients at the obstacle boundary and in the interior layer upstream of the goal point are well resolved, suggesting that the adaptive procedure successfully allocates refinement to regions with the highest influence on the goal functional. The width of the interior layer,

$$y_{\text{layer}} = y_1 - y_0, \quad (69)$$

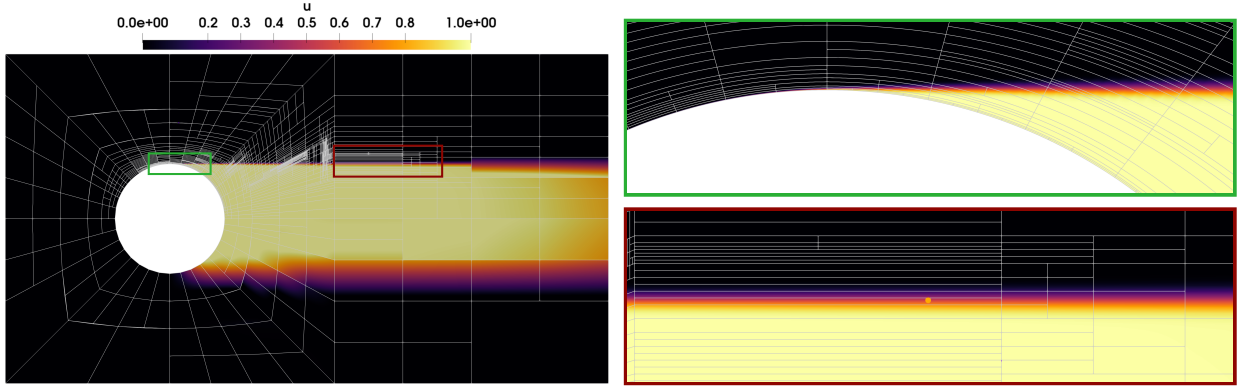


Figure 7: The solution to the Hemker problem with $\varepsilon = 10^{-4}$ in the final DWR loop. One can clearly see the adaptive mesh refinement at x_c and upstream of the point due to the goal (68).

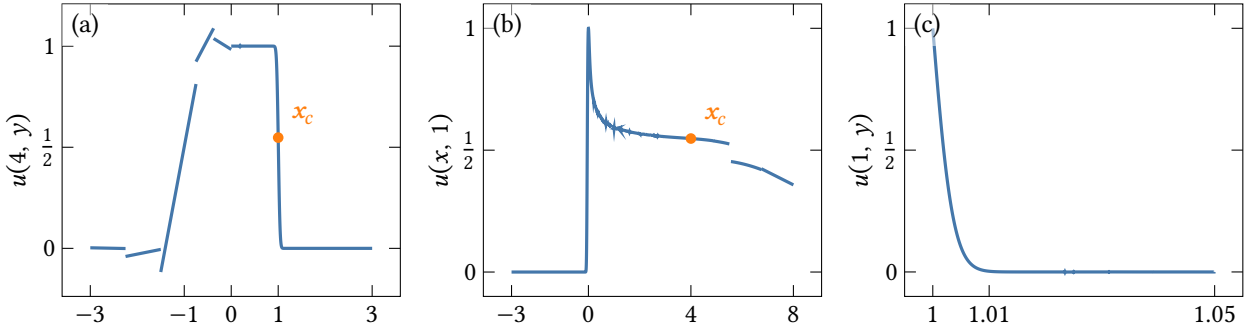


Figure 8: Cut lines of the solution to the Hemker problem with $\varepsilon = 10^{-4}$. In (a) a cut through the interior layers is plotted. In (b), the solution within the upper interior layer is plotted. In both cases we mark the control point which we use for the goal oriented error control. In (c) a cut through the boundary layer is plotted.

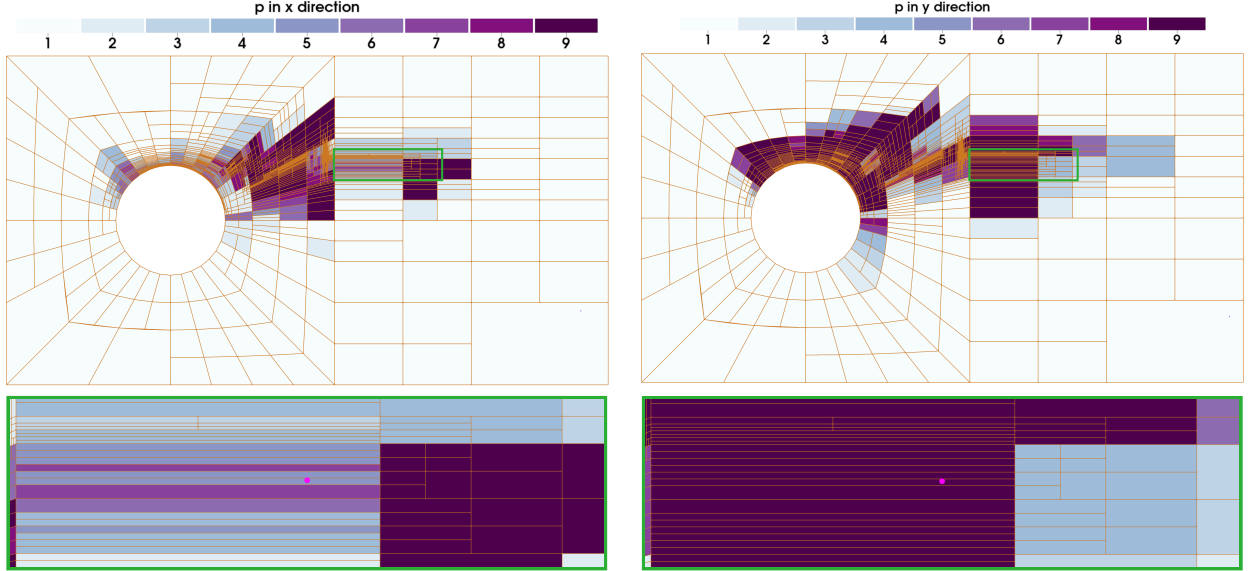


Figure 9: Anisotropic hp -mesh with polynomial degrees in x -direction (left) and y -direction (right) after 17 refinement steps for the Hemker problem with $\varepsilon = 10^{-4}$. Within the mesh we observe high anisotropies in the mesh size and polynomial degree.

Table 5: Number of DoFs, error estimators, error, and effectivity index for the Hemker benchmark with point value control (68) and diffusion coefficient $\varepsilon = 10^{-6}$.

ℓ	$ \mathcal{T}_h $	N_x^{lo}	N_x^{ho}	N_t	work	ρ_{\max}	$\eta_{h,1}$	$\eta_{h,2}$	η_h^a	η_τ	$\eta_{\tau h}^a$
0	160	640	1440	8	$1.02 \cdot 10^4$	4.10	$-6.67 \cdot 10^{-4}$	$2.46 \cdot 10^{-4}$	$-4.21 \cdot 10^{-4}$	$7.16 \cdot 10^{-5}$	$-3.49 \cdot 10^{-4}$
1	168	775	1659	8	$1.24 \cdot 10^4$	4.60	$-5.41 \cdot 10^{-3}$	$-4.15 \cdot 10^{-3}$	$-9.56 \cdot 10^{-3}$	$-1.69 \cdot 10^{-2}$	$-2.65 \cdot 10^{-2}$
2	175	928	1891	8	$1.48 \cdot 10^4$	4.60	$-7.25 \cdot 10^{-3}$	$-3.72 \cdot 10^{-3}$	$-1.10 \cdot 10^{-2}$	$-1.70 \cdot 10^{-2}$	$-2.80 \cdot 10^{-2}$
3	187	1171	2256	8	$1.87 \cdot 10^4$	6.70	$-3.15 \cdot 10^{-3}$	$5.02 \cdot 10^{-4}$	$-2.64 \cdot 10^{-3}$	$-1.92 \cdot 10^{-2}$	$-2.19 \cdot 10^{-2}$
4	203	1433	2660	8	$2.29 \cdot 10^4$	$1.21 \cdot 10^1$	$-2.68 \cdot 10^{-3}$	$-4.28 \cdot 10^{-4}$	$-3.11 \cdot 10^{-3}$	$-2.02 \cdot 10^{-2}$	$-2.33 \cdot 10^{-2}$
5	210	1688	3019	9	$5.06 \cdot 10^4$	$1.33 \cdot 10^1$	$3.92 \cdot 10^{-4}$	$6.26 \cdot 10^{-4}$	$1.02 \cdot 10^{-3}$	$-1.38 \cdot 10^{-2}$	$-1.28 \cdot 10^{-2}$
6	224	2137	3651	9	$6.41 \cdot 10^4$	$1.33 \cdot 10^1$	$4.01 \cdot 10^{-4}$	$7.27 \cdot 10^{-4}$	$1.13 \cdot 10^{-3}$	$-1.38 \cdot 10^{-2}$	$-1.27 \cdot 10^{-2}$
7	239	2601	4309	9	$7.80 \cdot 10^4$	$2.67 \cdot 10^1$	$5.92 \cdot 10^{-4}$	$1.49 \cdot 10^{-4}$	$7.41 \cdot 10^{-4}$	$-1.36 \cdot 10^{-2}$	$-1.29 \cdot 10^{-2}$
8	253	3150	5064	9	$9.45 \cdot 10^4$	$2.67 \cdot 10^1$	$5.78 \cdot 10^{-4}$	$4.61 \cdot 10^{-4}$	$1.04 \cdot 10^{-3}$	$-1.35 \cdot 10^{-2}$	$-1.25 \cdot 10^{-2}$
9	290	4748	7206	9	$1.42 \cdot 10^5$	$2.67 \cdot 10^1$	$1.72 \cdot 10^{-5}$	$-2.23 \cdot 10^{-4}$	$-2.06 \cdot 10^{-4}$	$-1.50 \cdot 10^{-2}$	$-1.52 \cdot 10^{-2}$
10	349	7241	10 601	10	$3.84 \cdot 10^5$	$2.67 \cdot 10^1$	$4.77 \cdot 10^{-8}$	$1.51 \cdot 10^{-5}$	$1.52 \cdot 10^{-5}$	$-1.35 \cdot 10^{-2}$	$-1.34 \cdot 10^{-2}$
14	843	41 144	53 396	12	$3.95 \cdot 10^6$	$5.33 \cdot 10^1$	$-3.28 \cdot 10^{-5}$	$1.49 \cdot 10^{-4}$	$1.16 \cdot 10^{-4}$	$-1.52 \cdot 10^{-3}$	$-1.41 \cdot 10^{-3}$
15	1057	58 657	75 020	12	$5.87 \cdot 10^6$	$1.07 \cdot 10^2$	$-4.47 \cdot 10^{-5}$	$1.34 \cdot 10^{-4}$	$8.96 \cdot 10^{-5}$	$-1.54 \cdot 10^{-3}$	$-1.45 \cdot 10^{-3}$
16	1317	81 577	103 094	12	$8.65 \cdot 10^6$	$2.13 \cdot 10^2$	$1.39 \cdot 10^{-6}$	$-2.81 \cdot 10^{-5}$	$-2.67 \cdot 10^{-5}$	$-1.55 \cdot 10^{-3}$	$-1.58 \cdot 10^{-3}$

is defined to be the length of the interval $[y_0, y_1]$ in which the solution falls from $u(4, y_0) = 0.9$ to $u(4, y_1) = 0.1$. John et al. [7] provide a reference value of $y_{\text{layer}} = 0.0723$, which we achieve exactly in the 17th DWR loop at only 62 682 spatial degrees of freedom (cf. Tab. 4).

The meshes in Fig. 9 show high anisotropy: along the convection direction the polynomial degree is predominantly increased, whereas in the transverse direction refinement is primarily performed in h . This directional refinement pattern is in line with expectations for convection-dominated problems, where p -refinement along the flow direction and h -refinement across thin layers are expected to be most efficient. The observed behavior indicates that the adaptive hp -strategy concentrates refinement in regions most relevant for the goal functional while selecting refinement types appropriate for the local solution structure.

9.3 Fichera Corner

The Fichera corner problem introduces boundary layers within the three-dimensional domain Ω given by $\Omega = (-1, 1)^3 \setminus [0, 1]^3$, which has a re-entrant corner at the origin $(0, 0, 0)$. The problem is defined by an initial concentration $u(x, 0) = \prod_{d=1}^3 \left[\frac{1}{4} (1 + \tanh(\frac{x_d+1}{\varepsilon})) (1 - \tanh(\frac{x_d-1}{\varepsilon})) \right]$, which is advected by the convection field $\mathbf{b} = (1, 1, 1)$ towards the singularity at the origin over an interval $I = (0, 1]$. This presents significant numerical challenges due to singularities and steep gradients near the boundary. The diffusion is set to $\varepsilon = 5.0 \cdot 10^{-4}$ and the reaction coefficient is given by $\alpha = 0$. Despite the moderate diffusion parameter, the elliptic nature of the corner singularity exacerbates the problem's complexity, rendering it a challenging benchmark for the numerical methods. Homogeneous Dirichlet boundary conditions are imposed on the three faces adjacent to the origin, while homogeneous Neumann conditions are enforced on all other boundary faces (cf. Fig. 10). The aim is to control the error within a control point $\mathbf{x}_c = (-10^{-4}, 0.25, -10^{-4})$ in the boundary layer near an edge. To this end, we use the goal functional

$$J(u) = u(\mathbf{x}_c, T), \quad (70)$$

which is defined analogous to (68). In space and time, the refinement fraction is set to $\theta_{\text{space}}^{\text{ref}} = \frac{1}{7}$ and $\theta_{\text{time}}^{\text{ref}} = \frac{1}{8}$. The coarsening fraction is set to $\theta_{\text{space}}^{\text{co}} = \theta_{\text{time}}^{\text{co}} = \frac{1}{25}$. We use polynomial degrees $1 \leq p \leq 5$ and $0 \leq k \leq 5$ in space and time, respectively. The initial space-time triangulation consists of a single cell in time and a once uniformly refined spatial coarse mesh (cf. Fig. 10).

Fig. 11 shows the solutions after 14 DWR loops at final time. We observe that the initial concentration has been transported towards the corner and edge singularities. Tab. 6 summarizes the adaptive refinement

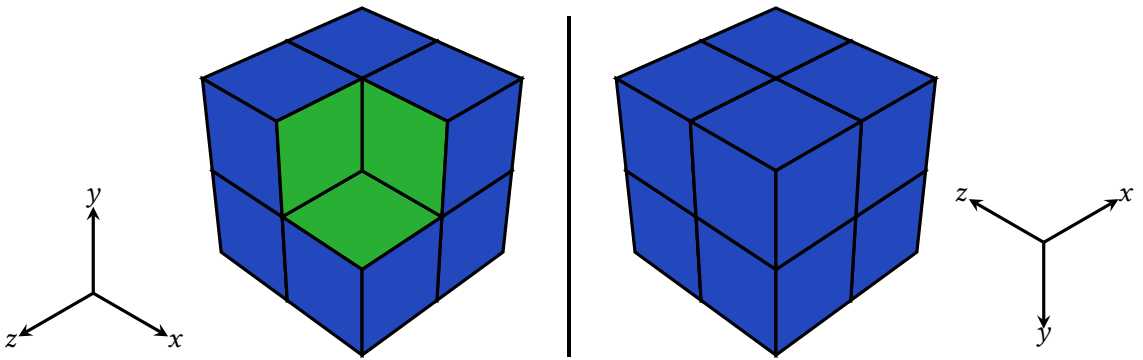


Figure 10: Geometry and coarse mesh of the Fichera cube. We depict views towards the origin $(0, 0, 0)$ in the direction $(-1, -1, -1)$ (left) and in the opposite direction $(1, 1, 1)$ (right). Green coloring corresponds to homogeneous Dirichlet BCs, while blue indicates homogeneous Neumann BCs.

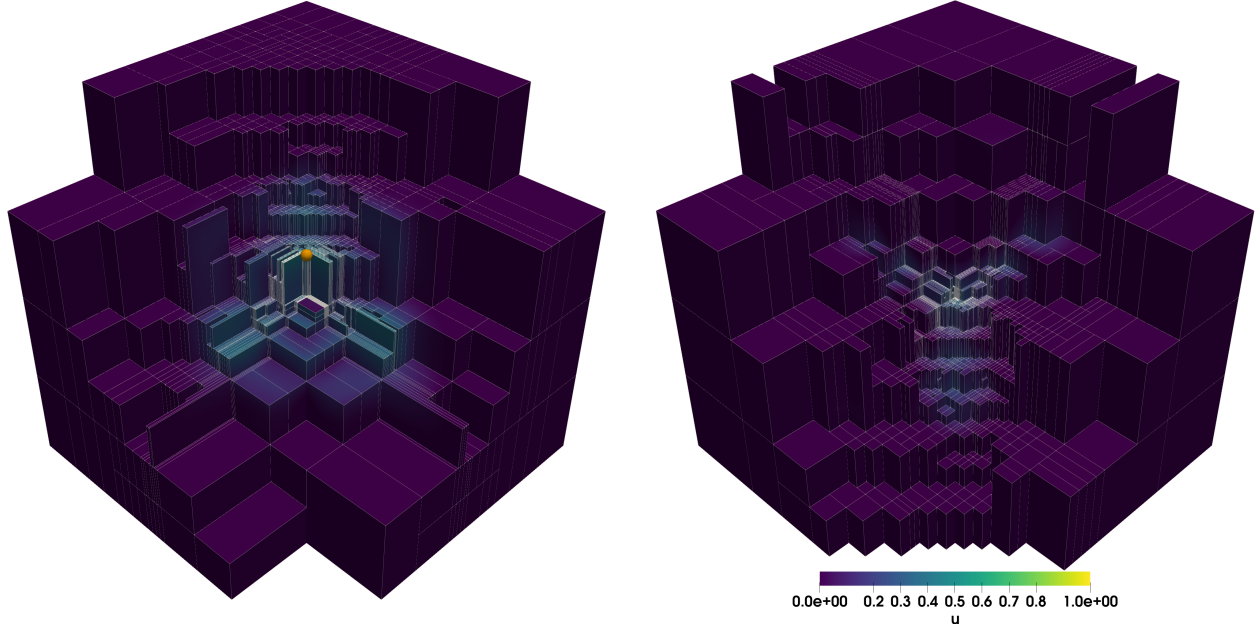


Figure 11: Solution and adapted mesh of the Fichera cube example. The depicted views are the same as above in Fig. 10. The point x_c is marked in orange

for the Fichera corner problem. As the DWR algorithm progresses, the number of cells grows, reflecting the need to resolve the singularities with h -refinement. The maximal anisotropy ρ_{\max} increases up to 512, showing that the algorithm strongly exploits directional refinement. The combined space-time error estimate $\eta_{\tau h}^a$ consistently decreases, indicating that the goal-oriented hp adaptive strategy remains effective despite the reduced regularity. These results demonstrate that the anisotropic hp -adaptivity can handle geometric singularities, where purely isotropic refinement would be far less efficient.

Fig. 12 shows the polynomial degree distributions in x -, y -, and z -direction (columns) together with clipped views (rows). The plots demonstrate that the adaptive strategy is impacted by the edge and corner singularities, where h -refinement is employed. This shows that the anisotropic hp -adaptive approach is capable of efficiently capturing the reduced regularity close to edges and corners.

Finally, let l and k be two cut lines starting at the boundary points

$$\mathbf{x}_l = (0, \frac{1}{4}, 0)^\top, \mathbf{x}_k = (0, \frac{1}{4} + 10^{-4}, 0)^\top \text{ with directions } \mathbf{d}_l = \frac{1}{\sqrt{2}}(-1, 0, -1)^\top, \mathbf{d}_k = \frac{1}{\sqrt{3}}(-1, -1, -1)^\top.$$

Table 6: Number of DoFs, error estimators, error, and effectivity indices for the Fichera corner problem with point value control (70) and diffusion coefficient $\varepsilon = 5.0 \cdot 10^{-4}$.

ℓ	$ \mathcal{T}_h $	N_x^{lo}	N_x^{ho}	N_t	work	ρ_{\max}	$\eta_{h,1}$	$\eta_{h,2}$	$\eta_{h,3}$	η_h^{a}	η_{τ}	$\eta_{\tau h}^{\text{a}}$
0	56	448	1512	1	$8.96 \cdot 10^2$	1.00	$2.58 \cdot 10^{-3}$	$-1.53 \cdot 10^{-3}$	$2.58 \cdot 10^{-3}$	$3.63 \cdot 10^{-3}$	$-9.78 \cdot 10^{-2}$	$-9.42 \cdot 10^{-2}$
1	56	556	1746	2	$1.11 \cdot 10^4$	1.00	$2.77 \cdot 10^{-3}$	$2.59 \cdot 10^{-3}$	$2.77 \cdot 10^{-3}$	$8.13 \cdot 10^{-3}$	$-4.73 \cdot 10^{-2}$	$-3.91 \cdot 10^{-2}$
2	56	695	2027	2	$1.39 \cdot 10^4$	1.00	$3.74 \cdot 10^{-3}$	$1.79 \cdot 10^{-3}$	$3.74 \cdot 10^{-3}$	$9.28 \cdot 10^{-3}$	$-5.15 \cdot 10^{-2}$	$-4.22 \cdot 10^{-2}$
3	64	972	2670	3	$3.79 \cdot 10^4$	2.00	$1.90 \cdot 10^{-3}$	$1.65 \cdot 10^{-3}$	$2.26 \cdot 10^{-3}$	$5.81 \cdot 10^{-3}$	$-2.03 \cdot 10^{-3}$	$3.79 \cdot 10^{-3}$
4	66	1207	3150	3	$4.71 \cdot 10^4$	2.00	$1.95 \cdot 10^{-3}$	$5.74 \cdot 10^{-4}$	$2.71 \cdot 10^{-3}$	$5.23 \cdot 10^{-3}$	$-1.99 \cdot 10^{-3}$	$3.25 \cdot 10^{-3}$
5	73	1638	4058	3	$6.39 \cdot 10^4$	2.00	$1.65 \cdot 10^{-3}$	$9.08 \cdot 10^{-4}$	$2.31 \cdot 10^{-3}$	$4.86 \cdot 10^{-3}$	$-1.16 \cdot 10^{-4}$	$4.75 \cdot 10^{-3}$
6	134	3731	8760	3	$1.46 \cdot 10^5$	4.00	$-2.18 \cdot 10^{-4}$	$2.20 \cdot 10^{-4}$	$-3.67 \cdot 10^{-4}$	$-3.66 \cdot 10^{-4}$	$-3.91 \cdot 10^{-3}$	$-4.28 \cdot 10^{-3}$
7	277	11121	23981	3	$4.34 \cdot 10^5$	8.00	$4.39 \cdot 10^{-5}$	$-1.94 \cdot 10^{-5}$	$-1.45 \cdot 10^{-4}$	$-1.12 \cdot 10^{-4}$	$-5.83 \cdot 10^{-3}$	$-5.95 \cdot 10^{-3}$
8	503	21835	46560	3	$8.52 \cdot 10^5$	$1.60 \cdot 10^1$	$-7.43 \cdot 10^{-6}$	$-1.37 \cdot 10^{-6}$	$-2.33 \cdot 10^{-4}$	$-2.42 \cdot 10^{-4}$	$-5.94 \cdot 10^{-3}$	$-6.18 \cdot 10^{-3}$
9	812	42199	86481	3	$1.65 \cdot 10^6$	$3.20 \cdot 10^1$	$-5.37 \cdot 10^{-5}$	$-1.06 \cdot 10^{-4}$	$-1.78 \cdot 10^{-4}$	$-3.38 \cdot 10^{-4}$	$-4.67 \cdot 10^{-3}$	$-5.01 \cdot 10^{-3}$
10	1438	87733	173442	3	$3.42 \cdot 10^6$	$6.40 \cdot 10^1$	$2.61 \cdot 10^{-5}$	$3.75 \cdot 10^{-5}$	$-9.81 \cdot 10^{-5}$	$-3.44 \cdot 10^{-5}$	$-2.23 \cdot 10^{-3}$	$-2.26 \cdot 10^{-3}$
11	2873	214811	407097	3	$8.38 \cdot 10^6$	$1.28 \cdot 10^2$	$3.65 \cdot 10^{-6}$	$1.98 \cdot 10^{-4}$	$-1.93 \cdot 10^{-5}$	$1.82 \cdot 10^{-4}$	$-5.22 \cdot 10^{-4}$	$-3.40 \cdot 10^{-4}$
12	6021	538839	988246	3	$2.10 \cdot 10^7$	$2.56 \cdot 10^2$	$3.83 \cdot 10^{-6}$	$1.12 \cdot 10^{-4}$	$-3.31 \cdot 10^{-6}$	$1.12 \cdot 10^{-4}$	$1.94 \cdot 10^{-3}$	$2.05 \cdot 10^{-3}$
13	11573	1172210	2101439	3	$4.57 \cdot 10^7$	$5.12 \cdot 10^2$	$2.73 \cdot 10^{-6}$	$7.56 \cdot 10^{-5}$	$-2.41 \cdot 10^{-6}$	$7.59 \cdot 10^{-5}$	$3.37 \cdot 10^{-4}$	$4.13 \cdot 10^{-4}$

We define their parametric forms

$$l(s) = \mathbf{x}_l + s\mathbf{d}_l, \quad s \in [0, 10^{-2}], \quad k(s) = \mathbf{x}_k + s\mathbf{d}_k, \quad s \in [0, \frac{1}{4}],$$

and the corresponding one-dimensional solution profiles

$$u_l(s) = u(l(s)), \quad u_k(s) = u(k(s)). \quad (71)$$

In Fig. 13 we plot $u_l(s)$ and $u_k(s)$ over s . The plots demonstrate that the solution remains smooth near the goal point \mathbf{x}_c , with the boundary layer being resolved by the underlying anisotropic hp -refined mesh. Further, the solution remains well-resolved downstream of \mathbf{x}_c due to the adaptive hp -refinement of regions that contribute to the goal functional.

10 Conclusion

We have presented a goal-oriented adaptive framework for convection-dominated transport problems based on a fully anisotropic space-time DG discretization with independent h - and p -updates in each spatial direction and in time, a directional DWR estimator yielding split indicators $\eta_{h,i}, \eta_{\tau}, i = 1, \dots, d$, and an h - and p -robust preconditioner for the resulting space-time systems. Our method leverages the Dual Weighted Residual approach to control the error with respect to user-defined target quantities and, by separating directional error contributions, applies h - or p -refinement independently in each spatial and temporal direction, thereby resolving thin boundary and interior layers and geometric singularities, concentrating computational effort where the goal functional is most sensitive, and maintaining solver robustness on highly anisotropic meshes and for high polynomial degrees.

To address the resulting large and potentially ill-conditioned linear systems, we proposed a preconditioner based on [8, 57], which shows good robustness with respect to both h - and p -refinement and performs well under strong anisotropies.

Numerical results for established benchmark problems in two and three dimensions confirm the accuracy and reliability of the proposed method. The approach consistently identifies and resolves boundary layers, interior layers, and geometric singularities such as those arising in the Fichera corner. The adaptive algorithm effectively concentrates resolution in regions that are most relevant for the chosen goal functional, leading to significant error reduction at moderate computational cost. For benchmarks with an

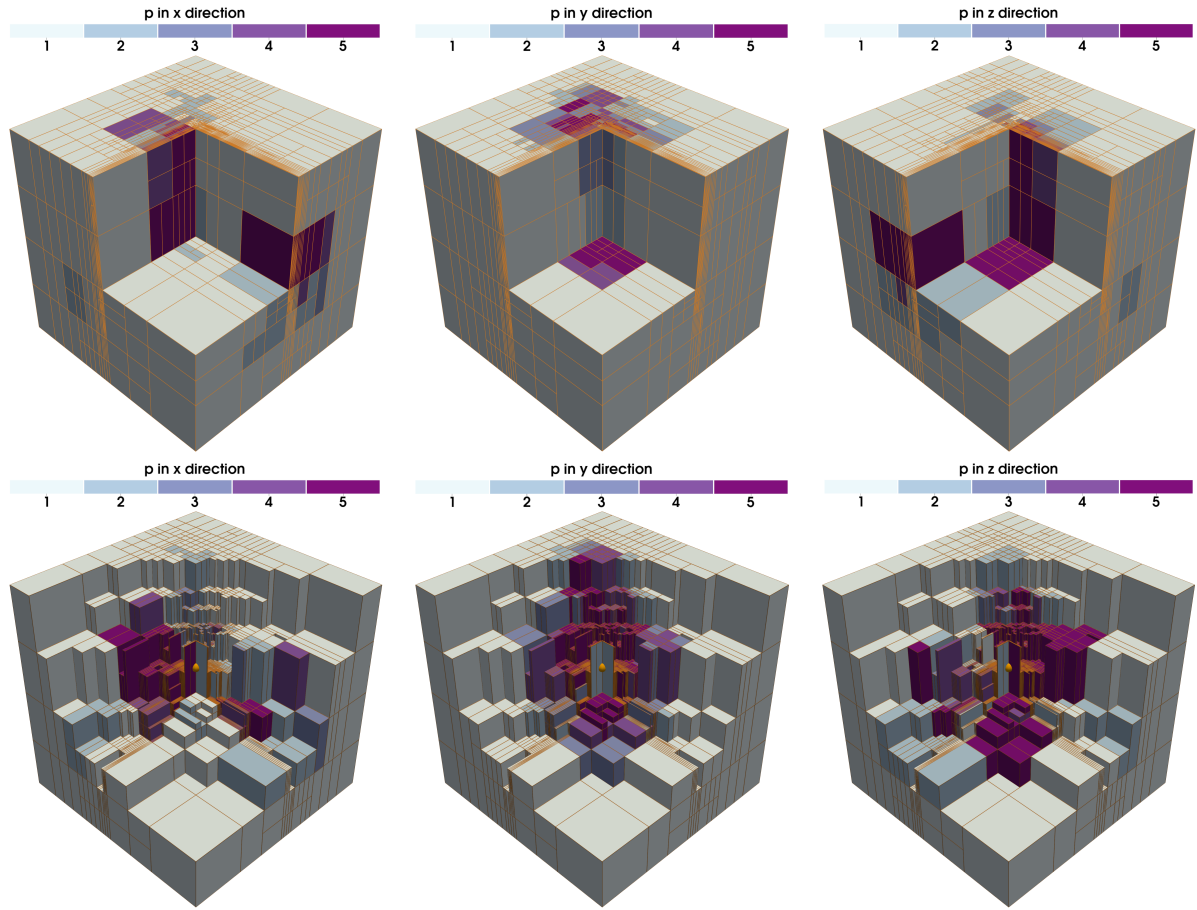


Figure 12: Polynomial degree distributions in x -, y -, and z -direction (columns), with two zoomed-in views for each direction (rows).

analytical solution we observed the expected exponential convergence of hp methods. Anisotropic refinement plays a critical role in resolving steep gradients along characteristic directions and capturing local features without unnecessary refinement elsewhere.

Overall, the results demonstrate that fully anisotropic hp -adaptivity combined with goal-oriented error control yields accurate and computationally efficient solutions for convection-dominated problems. Future work may focus on parallel mesh refinement, automated tuning of the decision criterion between h and p refinement, and nonlinear problems.

Acknowledgments Bernhard Endtmayer acknowledges the support by the Cluster of Excellence PhoenixD (EXC 2122, Project ID 390833453). Nils Margenberg acknowledges funding from the European Regional Development Fund (grant FEM Poer II, ZS?2024/06/18815) under the European Union's Horizon Europe Research and Innovation Program. Computational resources (HPC cluster HSUper) have been provided by the project hpc.bw, funded by dtec.bw - Digitalization and Technology Research Center of the Bundeswehr. dtec.bw is funded by the European Union - NextGenerationEU.

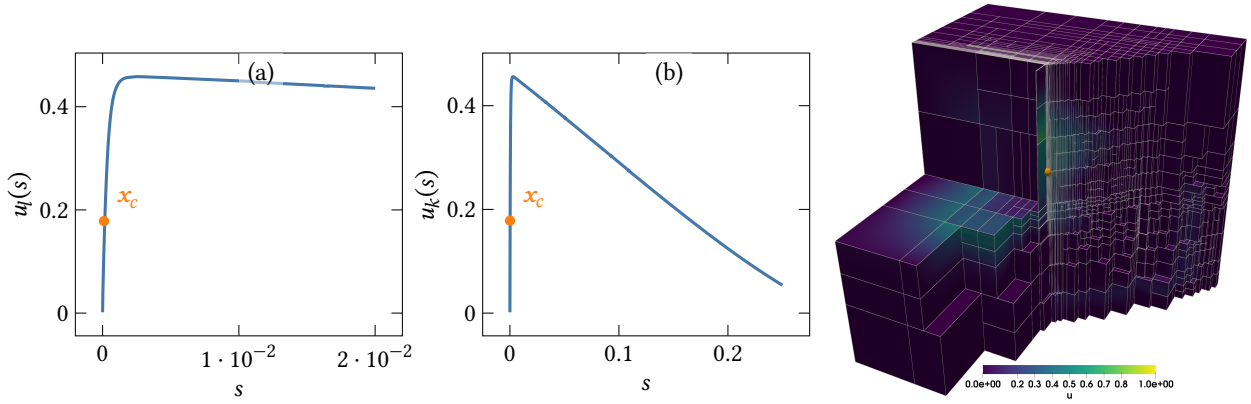


Figure 13: Cut lines of the solution to the Fichera corner problem. In (a) a cut orthogonal to the boundary is plotted. In (b) a cut through x_c in downstream direction of the convective field b is plotted (cf (71)). In both cases the control point which we use for the goal oriented error control is marked. On the right we plot another cut of the solution along the plane $(1, 0, -1)^\top$.

References

- [1] P. C. Africa et al. “The deal.II library, Version 9.6”. In: *Journal of Numerical Mathematics* 32.4 (2024), pp. 369–380. ISSN: 1569-3953. DOI: [10.1515/jnma-2024-0137](https://doi.org/10.1515/jnma-2024-0137).
- [2] N. Ahmed and V. John. “Adaptive time step control for higher order variational time discretizations applied to convection-diffusion equations”. In: *Comput. Methods Appl. Mech. Eng.* 285 (2015), pp. 83–101. DOI: [10.1016/j.cma.2014.10.054](https://doi.org/10.1016/j.cma.2014.10.054).
- [3] M. Ainsworth and B. Senior. “Aspects of an adaptive hp -finite element method: Adaptive strategy, conforming approximation and efficient solvers”. In: *Computer Methods in Applied Mechanics and Engineering. Symposium on Advances in Computational Mechanics* 150.1 (1997), pp. 65–87. ISSN: 0045-7825. DOI: [10.1016/S0045-7825\(97\)00101-1](https://doi.org/10.1016/S0045-7825(97)00101-1).
- [4] F. Alauzet, A. Belme, and A. Dervieux. “Anisotropic Goal-Oriented Mesh Adaptation for Time Dependent Problems”. In: *Proceedings of the 20th International Meshing Roundtable*. Ed. by W. R. Quadros. Berlin, Heidelberg: Springer, 2012, pp. 99–121. ISBN: 978-3-642-24734-7. DOI: [10.1007/978-3-642-24734-7_6](https://doi.org/10.1007/978-3-642-24734-7_6).
- [5] T. Apel. *Anisotropic finite elements: Local estimates and applications*. Advances in Numerical Mathematics. Teubner, Stuttgart, 1999.
- [6] T. Apel and G. Lube. “Anisotropic mesh refinement in stabilized Galerkin methods”. In: *Numerische Mathematik* 74.3 (1996), pp. 261–282. ISSN: 0945-3245. DOI: [10.1007/s002110050216](https://doi.org/10.1007/s002110050216).
- [7] M. Augustin et al. “An assessment of discretizations for convection-dominated convection–diffusion equations”. In: *Computer Methods in Applied Mechanics and Engineering* 200.47 (2011), pp. 3395–3409. ISSN: 0045-7825. DOI: [10.1016/j.cma.2011.08.012](https://doi.org/10.1016/j.cma.2011.08.012).
- [8] O. Axelsson and M. Neytcheva. “Numerical solution methods for implicit Runge-Kutta methods of arbitrarily high order”. In: *Proceedings of the Conference Algoritmy* (2020), pp. 11–20. URL: <http://www.iam.fmph.uniba.sk/amuc/ojs/index.php/algoritmy/article/view/1546>.
- [9] I. Babuška and B. Q. Guo. “Approximation properties of the h - p version of the finite element method”. In: *Computer Methods in Applied Mechanics and Engineering* 133.3 (1996), pp. 319–346. ISSN: 0045-7825. DOI: [10.1016/0045-7825\(95\)00946-9](https://doi.org/10.1016/0045-7825(95)00946-9).

[10] I. Babuška and M. R. Dorr. “Error estimates for the combined h and p versions of the finite element method”. In: *Numerische Mathematik* 37.2 (1981), pp. 257–277. ISSN: 0945-3245. doi: [10.1007/BF01398256](https://doi.org/10.1007/BF01398256).

[11] I. Babuška and M. Suri. “The p and h-p Versions of the Finite Element Method, Basic Principles and Properties”. In: *SIAM Review* 36.4 (Dec. 1994). Publisher: Society for Industrial and Applied Mathematics, pp. 578–632. ISSN: 0036-1445. doi: [10.1137/1036141](https://doi.org/10.1137/1036141).

[12] W. Bangerth, M. Geiger, and R. Rannacher. “Adaptive Galerkin Finite Element Methods for the Wave Equation”. In: *Computational Methods in Applied Mathematics* 10.1 (2010), pp. 3–48. doi: [10.2478/cmam-2010-0001](https://doi.org/10.2478/cmam-2010-0001).

[13] W. Bangerth and R. Rannacher. *Adaptive Finite Element Methods for Differential Equations*. Basel: Birkhäuser Verlag, 2003.

[14] W. Bangerth and O. Kayser-Herold. “Data Structures and Requirements for hp Finite Element Software”. In: *ACM Trans. Math. Softw.* 36.1 (2009), pp. 4/1–4/31.

[15] M. Bause et al. “Anisotropic space-time goal-oriented error control and mesh adaptivity for convection-diffusion-reaction equations”. In: *Preprint* (2025). doi: [10.48550/arXiv.2504.04951](https://doi.org/10.48550/arXiv.2504.04951).

[16] M. Bause et al. “Multi-goal-oriented anisotropic error control and mesh adaptivity for time-dependent convection-dominated problems”. In: (2025). URL: <https://arxiv.org/abs/2507.00723>.

[17] R. Becker and R. Rannacher. “An optimal control approach to a posteriori error estimation in finite element methods”. In: *Acta Numer.* 10 (2001), pp. 1–102. ISSN: 0962-4929.

[18] R. Becker and R. Rannacher. “Weighted a posteriori error control in FE methods”. In: *Lecture ENUMATH-95, Paris, Sept. 18-22, 1995, in: Proc. ENUMATH-97, Heidelberg, Sept. 28 - Oct.3, 1997 (H.G. Bock, et al., eds)*. pp. 621–637, World Sci. Publ., Singapore, 1998.

[19] M. Besier and R. Rannacher. “Goal-oriented space-time adaptivity in the finite element Galerkin method for the computation of nonstationary incompressible flow”. In: *Int. J. Num. Methods Fluids* 70.9 (2012), pp. 1139–1166. doi: [10.1002/fld.2735](https://doi.org/10.1002/fld.2735).

[20] M. Bittl and D. Kuzmin. “An hp-adaptive flux-corrected transport algorithm for continuous finite elements”. In: *Computing* 95. Suppl 1 (2013), pp. 27–48. doi: [10.1007/s00607-012-0223-y](https://doi.org/10.1007/s00607-012-0223-y).

[21] M. P. Bruchhäuser. “Goal-oriented space-time adaptivity for a multirate approach to coupled flow and transport”. PhD thesis. Helmut-Schmidt-University/University of the German Federal Armed Forces Hamburg, 2022. doi: [10.24405/14380](https://doi.org/10.24405/14380).

[22] M. P. Bruchhäuser and M. Bause. “Numerical Study of Approximation Techniques for the Temporal Weights to the DWR Method”. In: *Numerical Mathematics and Advanced Applications ENUMATH 2023, Volume 1*. Ed. by A. Sequeira et al. Cham: Springer Nature Switzerland, 2025, pp. 177–187.

[23] M. P. Bruchhäuser, U. Köcher, and M. Bause. “On the Implementation of an Adaptive Multirate Framework for Coupled Transport and Flow”. In: *Journal of Scientific Computing* 93.59 (2022). doi: [10.1007/s10915-022-02026-z](https://doi.org/10.1007/s10915-022-02026-z).

[24] M. P. Bruchhäuser, K. Schwegler, and M. Bause. “Dual Weighted Residual Based Error Control for Nonstationary Convection-Dominated Equations: Potential or Ballast?” In: *Boundary and Interior Layers, Computational and Asymptotic Methods BAIL 2018*. Ed. by G. R. Barrenechea and J. Mackenzie. Cham: Springer International Publishing, 2020, pp. 1–17.

[25] A. Cangiani et al. “hp-adaptive discontinuous Galerkin methods for non-stationary convection–diffusion problems”. In: *Computers & Mathematics with Applications* 78.9 (2019). Applications of Partial Differential Equations in Science and Engineering, pp. 3090–3104. ISSN: 0898-1221. doi: [10.1016/j.camwa.2019.04.002](https://doi.org/10.1016/j.camwa.2019.04.002).

[26] J. Carpio, J. L. Prieto, and R. Bermejo. “Anisotropic “Goal-Oriented” Mesh Adaptivity for Elliptic Problems”. In: *SIAM Journal on Scientific Computing* 35.2 (2013), A861–A885. doi: [10.1137/120874606](https://doi.org/10.1137/120874606).

[27] M. Ceze and K. J. Fidkowski. “Anisotropic hp-Adaptation Framework for Functional Prediction”. In: *AIAA Journal* 51.2 (Feb. 2013). Publisher: American Institute of Aeronautics and Astronautics (AIAA), pp. 492–509. ISSN: 0001-1452, 1533-385X. doi: [10.2514/1.j051845](https://doi.org/10.2514/1.j051845).

[28] A. Chakraborty, S. Henneking, and L. Demkowicz. “An anisotropic hp -adaptation framework for ultraweak discontinuous Petrov–Galerkin formulations”. In: *Computers & Mathematics with Applications* 167 (2024), pp. 315–327. ISSN: 0898-1221. doi: [10.1016/j.camwa.2024.05.025](https://doi.org/10.1016/j.camwa.2024.05.025).

[29] R. Dautray and J.-L. Lions. *Mathematical analysis and numerical methods for science and technology. Vol. 5: Evolution problems I. With the collaboration of Michel Artola, Michel Cessenat and Hélène Lanchon*. English. 2nd printing. Berlin: Springer, 2000. ISBN: 3-540-66101-8.

[30] L. Demkowicz, W. Rachowicz, and P. Devloo. “A Fully Automatic hp-Adaptivity”. In: *Journal of Scientific Computing* 17.1 (2002), pp. 117–142. ISSN: 1573-7691. doi: [10.1023/A:1015192312705](https://doi.org/10.1023/A:1015192312705).

[31] L. Demkowicz. *Computing with hp-ADAPTIVE FINITE ELEMENTS: Volume 1 One and Two Dimensional Elliptic and Maxwell Problems*. New York: Chapman and Hall/CRC, 2006. 398 pp. ISBN: 978-0-429-14037-2. doi: [10.1201/9781420011685](https://doi.org/10.1201/9781420011685).

[32] P. Devloo. “Object oriented tools for scientific computing”. In: *Engineering with Computers* 16 (2000), pp. 63–72. doi: [10.1007/s003660050037](https://doi.org/10.1007/s003660050037).

[33] V. Dolejší and G. May. “An Anisotropic hp-mesh Adaptation Method for Time-Dependent Problems Based on Interpolation Error Control”. In: *Journal of Scientific Computing* 95.2 (2023), p. 36. ISSN: 1573-7691. doi: [10.1007/s10915-023-02153-1](https://doi.org/10.1007/s10915-023-02153-1).

[34] B. Endtmayer, U. Langer, and T. Wick. “Two-Side a Posteriori Error Estimates for the Dual-Weighted Residual Method”. In: *SIAM Journal on Scientific Computing* 42.1 (2020), A371–A394. doi: [10.1137/18M1227275](https://doi.org/10.1137/18M1227275).

[35] B. Endtmayer, U. Langer, and A. Schafelner. “Goal-oriented adaptive space-time finite element methods for regularized parabolic p -Laplace problems”. In: *Computers & Mathematics with Applications* 167 (2024), pp. 286–297. ISSN: 0898-1221. doi: [10.1016/j.camwa.2024.05.017](https://doi.org/10.1016/j.camwa.2024.05.017).

[36] B. Endtmayer, U. Langer, and T. Wick. “Reliability and efficiency of DWR-type a posteriori error estimates with smart sensitivity weight recovering”. In: *Computational Methods in Applied Mathematics* 21.2 (2021), pp. 351–371. doi: [10.1515/cmam-2020-0036](https://doi.org/10.1515/cmam-2020-0036).

[37] B. Endtmayer et al. “Chapter Two - A posteriori single- and multi-goal error control and adaptivity for partial differential equations”. In: *Advances in Applied Mechanics*. Ed. by F. Chouly et al. Vol. 59. Error Control, Adaptive Discretizations, and Applications, Part 2. Elsevier, 2024, pp. 19–108. doi: [10.1016/bs.aams.2024.08.003](https://doi.org/10.1016/bs.aams.2024.08.003).

[38] A. Ern and F. Schieweck. “Discontinuous Galerkin method in time combined with a stabilized finite element method in space for linear first-order PDEs”. In: *Mathematics of Computation* 85.301 (2016), pp. 2099–2129. ISSN: 0025-5718, 1088-6842. doi: [10.1090/mcom/3073](https://doi.org/10.1090/mcom/3073).

[39] M. Fehling and W. Bangerth. “Algorithms for Parallel Generic hp -Adaptive Finite Element Software”. In: *ACM Transactions on Mathematical Software* 49.3 (2023), pp. 1–26. ISSN: 0098-3500, 1557-7295. doi: [10.1145/3603372](https://doi.org/10.1145/3603372).

[40] L. Formaggia, S. Micheletti, and S. Perotto. “Anisotropic mesh adaptation in computational fluid dynamics: Application to the advection–diffusion–reaction and the Stokes problems”. In: *Applied Numerical Mathematics. Applied Scientific Computing: Advances in Grid Generatuion, Approximation and Numerical Modeling* 51.4 (2004), pp. 511–533. ISSN: 0168-9274. doi: [10.1016/j.apnum.2004.06.007](https://doi.org/10.1016/j.apnum.2004.06.007).

[41] L. Formaggia, S. Perotto, and P. Zunino. “An anisotropic a-posteriori error estimate for a convection-diffusion problem”. In: *Computing and Visualization in Science* 4.2 (2001), pp. 99–104. ISSN: 1432-9360. DOI: [10.1007/s007910100061](https://doi.org/10.1007/s007910100061).

[42] E. H. Georgoulis, E. Hall, and P. Houston. “Discontinuous Galerkin Methods for Advection-Diffusion-Reaction Problems on Anisotropically Refined Meshes”. In: *SIAM Journal on Scientific Computing* (2007). Publisher: Society for Industrial and Applied Mathematics. DOI: [10.1137/060672352](https://doi.org/10.1137/060672352).

[43] E. H. Georgoulis, E. Hall, and P. Houston. “Discontinuous Galerkin methods on hp-anisotropic meshes I: a priori error analysis”. In: *International Journal of Computing Science and Mathematics* (2008). Publisher: Inderscience Publishers.

[44] E. H. Georgoulis, E. Hall, and P. Houston. “Discontinuous Galerkin methods on hp -anisotropic meshes II: a posteriori error analysis and adaptivity”. In: *Applied Numerical Mathematics*. Second Chilean Workshop on Numerical Analysis of Partial Differential Equations (WONAPDE 2007) 59.9 (2009), pp. 2179–2194. ISSN: 0168-9274. DOI: [10.1016/j.apnum.2008.12.008](https://doi.org/10.1016/j.apnum.2008.12.008).

[45] W. Gui and I. Babuška. “The h,p and $h\text{-}p$ versions of the finite element method in 1 dimension. Part 1: The error analysis of the p -version. Part 2: The error analysis of the h - and $h\text{-}p$ versions. Part 3: The adaptive $h\text{-}p$ version”. In: *Numer. Math.* 49.4 (1986), pp. 577–612, 613–657, 659–683. DOI: [10.1007/BF01389733](https://doi.org/10.1007/BF01389733).

[46] B. Guo and I. Babuška. “The $h\text{-}p$ version of the finite element method”. In: *Computational Mechanics* 1.1 (1986), pp. 21–41. ISSN: 1432-0924. DOI: [10.1007/BF00298636](https://doi.org/10.1007/BF00298636).

[47] B. Guo and I. Babuška. “The $h\text{-}p$ version of the finite element method”. In: *Computational Mechanics* 1.3 (1986), pp. 203–220. ISSN: 1432-0924. DOI: [10.1007/BF00272624](https://doi.org/10.1007/BF00272624).

[48] P. W. Hemker. “A singularly perturbed model problem for numerical computation”. In: *Journal of Computational and Applied Mathematics* 76.1 (1996), pp. 277–285. ISSN: 0377-0427. DOI: [10.1016/S0377-0427\(96\)00113-6](https://doi.org/10.1016/S0377-0427(96)00113-6).

[49] P. Houston, C. Schwab, and E. Süli. “Discontinuous hp-Finite Element Methods for Advection-Diffusion-Reaction Problems”. In: *SIAM Journal on Numerical Analysis* 39.6 (Jan. 2002). Publisher: Society for Industrial and Applied Mathematics, pp. 2133–2163. ISSN: 0036-1429. DOI: [10.1137/S0036142900374111](https://doi.org/10.1137/S0036142900374111).

[50] P. Houston, C. Schwab, and E. Süli. “Stabilized hp-Finite Element Methods for First-Order Hyperbolic Problems”. In: *SIAM Journal on Numerical Analysis* 37.5 (Jan. 2000). Publisher: Society for Industrial and Applied Mathematics, pp. 1618–1643. ISSN: 0036-1429. DOI: [10.1137/S0036142998348777](https://doi.org/10.1137/S0036142998348777).

[51] P. Houston and E. Süli. “A note on the design of hp -adaptive finite element methods for elliptic partial differential equations”. In: *Computer Methods in Applied Mechanics and Engineering*. Selected papers from the 11th Conference on The Mathematics of Finite Elements and Applications 194.2 (2005), pp. 229–243. ISSN: 0045-7825. DOI: [10.1016/j.cma.2004.04.009](https://doi.org/10.1016/j.cma.2004.04.009).

[52] V. John, P. Knobloch, and J. Novo. “Finite elements for scalar convection-dominated equations and incompressible flow problems: a never ending story?” In: *Computing and Visualization in Science* 19 (2018), pp. 47–63. DOI: [10.1007/s00791-018-0290-5](https://doi.org/10.1007/s00791-018-0290-5).

[53] P. Knobloch and R. Schneider. “On adaptive anisotropic mesh optimization for convection–diffusion problems”. In: *Journal of Computational and Applied Mathematics* 469 (2025), p. 116661. DOI: [10.1016/j.cam.2025.116661](https://doi.org/10.1016/j.cam.2025.116661).

[54] U. Köcher, M. P. Bruchhäuser, and M. Bause. “Efficient and scalable data structures and algorithms for goal-oriented adaptivity of space–time FEM codes”. In: *SoftwareX* 10 (2019), p. 100239.

[55] T. Leicht and R. Hartmann. “Error estimation and anisotropic mesh refinement for 3d laminar aerodynamic flow simulations”. In: *Journal of Computational Physics* 229.19 (2010), pp. 7344–7360. ISSN: 0021-9991. DOI: [10.1016/j.jcp.2010.06.019](https://doi.org/10.1016/j.jcp.2010.06.019).

[56] J. M. Melenk. *hp-Finite Element Methods for Singular Perturbations*. Lecture Notes in Mathematics. ISSN: 0075-8434, 1617-9692. Berlin, Heidelberg: Springer, 2002. doi: [10.1007/b84212](https://doi.org/10.1007/b84212).

[57] P. Munch et al. “Stage-Parallel Fully Implicit Runge–Kutta Implementations with Optimal Multilevel Preconditioners at the Scaling Limit”. In: *SIAM Journal on Scientific Computing* (2023). Publisher: Society for Industrial and Applied Mathematics, S71–S96. ISSN: 1064-8275. doi: [10.1137/22M1503270](https://doi.org/10.1137/22M1503270).

[58] J. T. Oden and S. Prudhomme. “Goal-oriented error estimation and adaptivity for the finite element method”. In: *Computers & Mathematics with Applications* 41.5 (2001), pp. 735–756. ISSN: 0898-1221. doi: [10.1016/S0898-1221\(00\)00317-5](https://doi.org/10.1016/S0898-1221(00)00317-5).

[59] R. Picard and D. McGhee. *Partial Differential Equations: A unified Hilbert Space Approach*. De Gruyter, 2011. ISBN: 978-3-11-025027-5. doi: [10.1515/9783110250275](https://doi.org/10.1515/9783110250275).

[60] M. Picasso. “Adaptive finite elements for a linear parabolic problem”. In: *Computer Methods in Applied Mechanics and Engineering* 167.3 (1998), pp. 223–237. ISSN: 0045-7825. doi: [10.1016/S0045-7825\(98\)00121-2](https://doi.org/10.1016/S0045-7825(98)00121-2).

[61] R. Rannacher and F.-T. Suttmeier. “A posteriori error estimation and mesh adaptation for finite element models in elasto-plasticity”. In: *Computer Methods in Applied Mechanics and Engineering* 176.1 (1999), pp. 333–361. doi: [10.1016/S0045-7825\(98\)00344-2](https://doi.org/10.1016/S0045-7825(98)00344-2).

[62] T. Richter and T. Wick. “Variational localizations of the dual weighted residual estimator”. In: *J. Comput. Appl. Math.* 279 (2015), pp. 192–208. ISSN: 0377-0427. doi: [10.1016/j.cam.2014.11.008](https://doi.org/10.1016/j.cam.2014.11.008).

[63] T. Richter. “Goal-oriented error estimation for fluid–structure interaction problems”. In: *Computer Methods in Applied Mechanics and Engineering* 223–224 (2012), pp. 28–42. doi: [10.1016/j.cma.2012.02.014](https://doi.org/10.1016/j.cma.2012.02.014).

[64] T. Richter. “A posteriori error estimation and anisotropy detection with the dual-weighted residual method”. In: *International Journal for Numerical Methods in Fluids* 62.1 (2010), pp. 90–118. ISSN: 1097-0363. doi: [10.1002/fld.2016](https://doi.org/10.1002/fld.2016).

[65] T. Richter, A. Springer, and B. Vexler. “Efficient numerical realization of discontinuous Galerkin methods for temporal discretization of parabolic problems”. In: *Numerische Mathematik* 124.1 (2013), pp. 151–182. ISSN: 0945-3245. doi: [10.1007/s00211-012-0511-7](https://doi.org/10.1007/s00211-012-0511-7).

[66] H.-G. Roos, M. Stynes, and L. Tobiska. *Robust numerical methods for singularly perturbed differential equations*. Berlin: Springer, 2008. doi: [10.1007/978-3-540-34467-4](https://doi.org/10.1007/978-3-540-34467-4).

[67] J. Roth et al. “Tensor-Product Space-Time Goal-Oriented Error Control and Adaptivity With Partition-of-Unity Dual-Weighted Residuals for Nonstationary Flow Problems”. In: *Comput. Methods Appl. Math.* 24.1 (2024), pp. 185–214. doi: [10.1515/cmam-2022-0200](https://doi.org/10.1515/cmam-2022-0200).

[68] M. Schmich and B. Vexler. “Adaptivity with dynamic meshes for space-time finite element discretizations of parabolic equations”. In: *SIAM J. Sci. Comput.* 30.1 (2008), pp. 369–393. doi: [10.1137/060670468](https://doi.org/10.1137/060670468).

[69] R. Schneider. “A Review of Anisotropic Refinement Methods for Triangular Meshes in FEM”. In: *Advanced Finite Element Methods and Applications*. Ed. by T. Apel and O. Steinbach. Berlin, Heidelberg: Springer Berlin Heidelberg, 2013, pp. 133–152. doi: [10.1007/978-3-642-30316-6_6](https://doi.org/10.1007/978-3-642-30316-6_6).

[70] C. Schwab. *p- and hp-Finite Element Methods: Theory and Applications in Solid and Fluid Mechanics*. Numerical Mathematics and Scientific Computation. Clarendon Press, Oxford University Press, 1998. ISBN: 978-0-19-850390-3.

[71] P. Šolín and L. Demkowicz. “Goal-oriented *hp*-adaptivity for elliptic problems”. In: *Computer Methods in Applied Mechanics and Engineering* 193.6 (2004), pp. 449–468. ISSN: 0045-7825. doi: [10.1016/j.cma.2003.09.015](https://doi.org/10.1016/j.cma.2003.09.015).

- [72] J. P. Thiele and T. Wick. “Numerical Modeling and Open-Source Implementation of Variational Partition-of-Unity Localizations of Space-Time Dual-Weighted Residual Estimators for Parabolic Problems”. In: *J. Sci. Comput.* 99.25 (2024).
- [73] D. A. Venditti and D. L. Darmofal. “Anisotropic grid adaptation for functional outputs: application to two-dimensional viscous flows”. In: *Journal of Computational Physics* 187.1 (2003), pp. 22–46. ISSN: 0021-9991. doi: [10.1016/S0021-9991\(03\)00074-3](https://doi.org/10.1016/S0021-9991(03)00074-3).
- [74] T. Werder et al. “*hp*-Discontinuous Galerkin time stepping for parabolic problems”. In: *Computer Methods in Applied Mechanics and Engineering* 190.49 (2001), pp. 6685–6708. ISSN: 0045-7825. doi: [10.1016/S0045-7825\(01\)00258-4](https://doi.org/10.1016/S0045-7825(01)00258-4).
- [75] T. Wick and W. Wollner. “Optimization with nonstationary, nonlinear monolithic fluid-structure interaction”. In: *International Journal for Numerical Methods in Engineering* 122.19 (2021), pp. 5430–5449. doi: [10.1002/nme.6372](https://doi.org/10.1002/nme.6372).